

Modeling CMAQ dry deposition treatment over Western Pacific: A distinct characteristic of mineral dust and anthropogenic aerosol

Steven Soon-Kai Kong¹, Joshua S. Fu², Neng-Huei Lin^{1,3,*}, Guey-Rong Sheu^{1,3,*}, Wei-Syun Huang¹

¹ Department of Atmospheric Sciences, National Central University, Taoyuan, 32001, Taiwan

² Department of Civil and Environmental Engineering, the University of Tennessee Knoxville, TN37996, USA

³ Center for Environmental Monitoring and Technology, National Central University, Taoyuan, 32001, Taiwan

Correspondence to: Neng-Huei Lin (nhlin@cc.ncu.edu.tw) and Guey-Rong Sheu (grsheu@atm.ncu.edu.tw)

Abstract. Dry deposition plays a vital role in the aerosol removal process from the atmosphere. However, the chemical transport model (CTM) is sensitive to the dry deposition parameterization and yet remains to be determined due to the limited particle deposition measurement. By utilizing the CMAQv5.4 with the refined dust emission treatment, the East Asian dust (EAD) simulation during January 2023 and Spring 2021 was constructed to evaluate the performance of dry deposition parameterizations, namely S22, E20, and P22. The result showed that the dry deposition parameterization could significantly impact the CMAQ dust emission treatment. By implementing the E20 dry deposition scheme, the CMAQ simulation performance of the surface PM₁₀ has been considerably improved with the NMB of -41.9 %, as compared to the dry deposition proposed by S22 (-47.01 %) and P22 (-53.90 %). The modeled PM₁₀ pattern by E20 at the upper level (700 hPa) was mostly consistent with the observed PM₁₀ at the Lulin Atmospheric Background Station (LABS; 23.47° N, 120.87° E; 2862 m a.s.l.) where is a typical background site at Western Pacific, particularly in capturing the peak value. The correlations (R) at the high-altitude were well performed for E20 by 0.55, as compared to S22 (0.54) and P22 (0.46). Moreover, E20 improved the simulated PM₁₀ concentrations and aerosol optical depth (AOD) value over the Asian Continental during the multiple dust episodes in spring 2021, by NMB of -25.43 % and -26.19 %, respectively. The noticeable deduction of the coarse mode particle's deposition velocity (V_d) was responsible for reducing the PM₁₀ simulation underestimation. On 22-31 January 2023, the *in-situ* measurement of the upper level observed the possibility of natural dust and anthropogenic aerosol. This is consistent with the CMAQ, which shows that both aerosol types displayed a clear "long dust-black

31 carbon belt" along the 15°N. It is revealed that the increase of wet deposition due to the surface resistivity
32 (R_b) leads to a significant increase in dust mass concentration but a minor increase in black carbon (BC).
33 We proposed implementing the E20 dry deposition approach, narrowing the uncertainty of the CMAQ
34 dust emission treatment.

35 1 Introduction

36 The chemical transport model (CTM) is a powerful tool for comprehending air pollution, encompassing
37 emission, transport, radiative impact, and removal mechanisms at various grid scales. Among
38 these, particle dry deposition is a crucial aerosol removal process and an important sink for particles in
39 the model. The derivation of the dry deposition is based on the resistance framework and
40 electrical analogue, but its implementation can vary across models (Wesley, 1989; Giardina and Buffa,
41 2018; Gaydos et al., 2007; Khan and Perlinger, 2017; Shu et al., 2017). A key challenge in dry deposition
42 simulation is the scarcity of measurement data for model verification, underscoring the necessity for
43 further research to enhance the accuracy of air quality modeling.

44 An immense range of dry deposition parameterization has been implanted in the model. The
45 deposition mechanism by Slinn (1982) includes the deposition process such as turbulent transfer,
46 Brownian diffusion, impaction, interception, gravitational settling, and particle rebound, where the
47 particle grows under humid conditions. Zhang et al. (2001) suggested the dry deposition scheme is
48 sensitive to land use category and several parameters. For instance, due to the particle growth, the
49 deposition velocity (V_d) over the ocean is much higher than on another land surface, as the V_d increased
50 rapidly with the increase of particle size. Some CTMs using Zhang et al. (2001) parameterization still
51 underestimated the global $PM_{2.5}$ concentration. The latest dry deposition scheme revision by Emerson et
52 al. (2020) based on the flux measurement of grassland and pine forest has reduced the uncertainty,
53 marking a significant step forward in our quest for more accurate air quality modeling.

54 An updated deposition scheme that reduces the dependence of the deposition velocity on the aerosol
55 mode width has been proposed (Shu et al., 2022). Indeed, the approach suggested that vegetation
56 dependence increased the V_d for submicrons and decreased for large particles by 37 % and -66 %,

57 respectively. It also reduced the functional biases by 56-97 % for vegetated land-use type and equivalence
58 performance over the water. Moreover, adding the second inertial impaction term for microscale obstacles
59 such as leaf hairs, microscale ridges, and needle leaf edge effects managed to increase the mass dry
60 deposition of the accumulation mode aerosols in the model (Pleim et al., 2022). These modifications
61 reduced the average $PM_{2.5}$ in the atmosphere during July 2018 over the contiguous United States.

62 With a plethora of deposition approaches in use, it becomes paramount to comprehend their impact
63 on model performance in predicting aerosol behaviour. The surface fine particle concentrations can vary
64 up to 5-15 %, and the particle dry deposition has more than 200 % discrepancy due to the different dry
65 deposition schemes. (Saylor et al., 2019). A comprehensive evaluation of five different parameterizations
66 has been conducted, with the simplest and most effective deposition mechanism suggested for the CTM
67 (Khan and Perlinger, 2017). However, the model's reliance on meteorological factors such as frictional
68 velocity, relative humidity, rainfall, or wind speed, which can significantly influence
69 the model's accuracy, remains a challenge (Kong et al., 2021).

70 Besides the model bias on $PM_{2.5}$, the simulation of PM_{10} has been underestimated due to the
71 uncertainty of the deposition mechanism, particularly over the western Pacific (Kong et al., 2021). The
72 V_d is overestimated for coarse particles, where the dry deposition velocity is too high for coarse particles
73 when the frictional velocity is large, which is why the surface PM_{10} concentration is underestimated (Ryu
74 and Min, 2022). The model performance of PM_{10} simulation that is widely influenced by the dust
75 treatment embedded within CMAQ has been revised (Dong et al., 2016; Liu et al., 2021; Kong et al.,
76 2021, 2024) and are found to effectively simulate the PM_{10} over the western Pacific region such as
77 Taiwan. However, the issue regarding the deposition algorithm's impact on the model performance at the
78 corresponding region needs to be discussed. The present research intends to evaluate the CMAQ model
79 performance due to the different deposition schemes on aerosols in the Taiwan region.

80 The model performance in Taiwan is paramount in our study, as the area is equipped with a substantial
81 number of well-maintained surface observation sites, providing comprehensive coverage. The LABS
82 station in the high-altitude subtropical western North Pacific region serves as the sole background station

83 for monitoring transboundary pollutants. This station is crucial in our research as it provides unique data
84 on the long-range transport of pollutants, further underscoring the relevance of our study.

85 The transboundary pollutants mechanisms have been widely discussed through LABS measurements,
86 cooperating with the backward trajectory, reanalysis dataset, and modeling approach. Previous research
87 reveals that LABS pollutants could be associated with severe fire emissions from northern Peninsular
88 Southeast Asia (Huang et al., 2020; Ooi et al., 2021) and Indonesia (Ravindra Babu et al., 2023).
89 Moreover, the intense wind speed in northwest China could transport the mineral dust through the surface
90 and high-altitude layer detected at LABS (Kong et al., 2021; Kong et al., 2022). Additionally, the transport
91 process of East Asian haze due to the cold surge from the Asian Continental industrial region towards
92 Taiwan has been widely discussed (Chuang et al., 2020). Instead of pure aerosol, the coexistence of dust
93 and biomass burning over Taiwan, a condition discovered in previous research, has significant
94 implications for the regional climate (Dong et al., 2018; Dong et al., 2019). However, the high-altitude
95 synoptic pattern associated with the coexistence between natural dust and anthropogenic pollutants
96 remains unknown due to a lack of observations at the upper layers.

97 This study used the chemical transport model to investigate the long-range transport of East Asian
98 dust (EAD) that occurred on 22-31 January 2023 and 12 March-20 April 2021. Due to the limitation of
99 the dust model, the CMAQ version 5.4, embedded with three types of dry deposition schemes, was
100 implemented to justify the effectiveness of improving our latest refined dust model (Kong et al., 2024).
101 The dry deposition scheme proposed by Shu et al. (2022) has reduced certain model bias as compared to
102 the base scheme. However, the revised scheme response to the natural phenomenon such as wind-blown
103 dust has not being tested. In the other way, the number of concentrations of the large size particle has
104 been decreased over land, and increased over ocean area globally by the adjusted collective coefficient
105 proposed by Emerson et al. (2020). Pleim et al. (2022) has included the consideration of white cap effect
106 which dependent on wind speed and sea surface temperature into the dry deposition scheme. Hence, the
107 response of the CMAQ dust model under the newly developed dry deposition schemes are worth
108 investigating in reducing the model uncertainty.

LABS detected the recent transboundary episode in January 2023 as a mixing aerosol type (see Section 3.1), which has not been widely discussed, and the multiple dust storm episodes mentioned by Kong et al. (2024) provide an opportunity to model the EAD over the downwind region. Recognizing the significant transboundary events detected through Taiwan's observations, the improvement of the CMAQ dust model by the dry deposition schemes, and its application in characterizing the transport mechanism can be vital. The paper is organized as follows. The model setup and ancillary datasets are discussed in Sect. 2. The results and discussion are presented in Sect. 3, followed by the conclusions in Sect. 4.

2 Data and Methodology

2.1 Dust emission treatment

Before delving into the details, it's important to understand the process of dust transport. Dust is primarily transported by wind through a process known as sandblasting (Kok et al., 2012). For dust to be uplifted, the horizontal wind speed must exceed a certain threshold frictional velocity ($u_{*,t}$), which is estimated by the model as follows:

$$u_{*,t} = u_{*,to} f_m f_r \quad (1)$$

Where $u_{*,to}$ is the ideal threshold friction velocity, while f_m and f_r are the correction factors of soil moisture and surface roughness, respectively.

Through a collaborative effort, the windspeed, soil texture, soil moisture, and surface roughness length derived from field and laboratory studies have been integrated into the windblown dust treatment, which is now a part of the Community Multiscale Air Quality (CMAQ) modeling system (Foroutan et al., 2017). This model, developed and evaluated over the continental United States, has also been extended to the East Asia region (Dong et al., 2016; Liu et al., 2021; Kong et al., 2021, 2024). Kong et al. (2024) have proposed further improvements, including the integration of the revised soil moisture fraction, dust emission speciation profile, and bulk soil density, to enhance the representation of the Asian dust simulation. This ongoing collaboration is crucial for the continuous improvement of our understanding and management of dust emissions.

134 2.2 Particle dry deposition schemes

135 Particle dry deposition is a complex process relating to the deposition velocity, particle size, source and
136 composition, land use surface, and meteorological condition. Generally, the flux of the particle mass
137 through the surface boundary layer is estimated as:

$$138 \quad F = C \times V_d \quad (2)$$

139 where F is the deposition flux, C is the particle concentration at the surface layer, and V_d is the deposition
140 velocity.

141 The difference in the particle concentration and deposition prediction among the various
142 atmospheric chemistry models was probably due to the algorithm of the dry deposition particle. The
143 algorithm describing particle deposition velocity as a function of particle size in almost all current air
144 quality model systems is descended from Slinn (1982). The particle deposition according to vegetative
145 canopies formulated the deposition velocity as:

$$146 \quad V_d = V_g + \frac{1}{R_a + R_b} \quad (3)$$

147 where V_g is the gravitation settling velocity, R_a is the resistivity aerodynamic, R_b is the surface resistivity,
148 also known as quasi-laminar sub-layer resistivity in STAGE. The V_s is calculated according to Stokes's
149 Law as:

$$150 \quad V_g = \frac{p_p D_p^2 g C_c}{18\eta} \quad (4)$$

151 where, p_p is the density of the particle; D_p is the diameter of the particle; g is gravitational acceleration;
152 C_c is the Cunningham correction factor for small particles; and, η is the dynamic viscosity of air.

153 CMAQ is embedded with M3Dry dry deposition calculation that implements the scheme of Pleim
154 and Ran (2011), which is based on Slinn (1982). As noted by Pleim and Ran (2011), chemical surface
155 flux modeling has become an essential process in the air quality model. For instance, the linkages of

156 ambient concentration levels to the deposition of SO_x and NO_x. Moreover, Surface Tiled Aerosol and
157 Gaseous Exchange (STAGE) deposition has been implemented within the CMAQv5.3, where estimated
158 fluxes from sub-grid cell fractional land-use values, aggregate the fluxes to the model grid cell and unifies
159 the bidirectional and unidirectional deposition schemes using the resistance framework (Massad et al.,
160 2010; Nemitz et al., 2001). The updated STAGE version in CMAQv5.4 could aggregate the grid-scale
161 values that match the grid-scale values from most kinds of Land Surface Model of WRF (Hogrefe et al.,
162 2023). Since the present study is primary focused on the impact of dry deposition scheme on CMAQ dust
163 model, the simulations with the STAGE module are the mandatory concern.

164 2.3 CMAQ model design

165 This study applied WRF v4.0 for the meteorological field parameters and CMAQv5.4 to simulate the
166 transboundary East Asian dust episodes on 22-31 January 2023, and the multiple dust storm episodes
167 during 12 March-20 April 2021. The modeling domain was set up to cover the Taklamakan and Gobi
168 Desert, with a resolution of 45 km, and nested towards Taiwan at a resolution of 15 km (d02) and 5 km
169 (d03) (Fig .1, Table 2). Also, as Taiwan is influenced by biomass burning, the domain covers up to the
170 peninsular Southeast Asia (PSEA), which will be carried out in the future (Ooi et al., 2021). The model
171 consisted of 40 vertical layers, with eight layers below ~1 KM altitude, 13 layers below ~3 KM altitude,
172 and 27 layers covering the upper layer to ~21 KM. The model's initial and lateral boundary
173 conditions were constructed using the National Centers for Environmental Prediction (NCEP) Final
174 Analyses (FNL) reanalysis dataset on a 0.5° × 0.5° grid. The data assimilation was conducted by grid
175 nudging in all the domains. The CB06 gas-phase chemical mechanism and the AERO7 aerosol module
176 model were implemented in CMAQ for the present study.

177 The anthropogenic emission inventories in East Asia, crucial for our research, were obtained from
178 the MICS-Asia (Model Inter-Comparison Study for Asia) Phase III emission inventory (Li et al., 2017).
179 The emissions of SO₂, NO_x, NMVOC, NH₃, CO, PM₁₀, PM_{2.5}, BC, OC and CO₂ has been meticulously
180 modified, taking into account of the relative changes in China's anthropogenic emissions between 2010
181 and 2017 (Zheng et al., 2018). Additionally, the modified emission of NO₂ was adjusted further by the
182 satellite imagery OMI-NO₂ in January 2023 (Huang et al., 2021). Biogenic emissions for Taiwan were

183 prepared by the Biogenic Emission Inventory System version 3.09 (BEIS3, Vukovich and Pierce, 2002)
184 and, for regions outside Taiwan, by the Model of Emissions of Gases and Aerosols from Nature v2.1
185 (MEGAN, Guenther et al., 2012). TEDS 10.0 (Taiwan Emission Database System, TWEPA, 2011;
186 <https://erdb.epa.gov.tw/>, last access: 18 January 2024) was used for domain 3 (d03). To ensure the
187 precision of the multiple dry deposition parameterizations, the present research conducted five simulation
188 scenarios, namely CMAQ_Off_S22, CMAQ_Dust_S22, CMAQ_Dust_E20 and CMAQ_Dust_P22. The
189 CMAQ_Off_S22 scenario did not include the inline dust calculation (Table 2). Meanwhile, the latest
190 refined integrated dust treatment was implemented in the CMAQ_Dust_S22 scenario (Kong et al., 2024).
191 Indeed, both CMAQ_Off_S22 and CMAQ_Dust_S22 used the dry deposition mechanism by Shu et al.
192 (2011). The dry deposition mechanism of Emerson et al. (2020) and Pleim et al. (2022) were implemented
193 in CMAQ_Dust_E20 and CMAQ_Dust_P22 scenarios, respectively.

194 V_d over the ocean surface has been shown to influence the CTMs in simulating aerosol,
195 particularly PM_{10} . The modeled PM_{10} can be increased by reducing V_d by a factor of 10 based on the bare
196 soil measurement (Tav et al., 2018; Ryu et al., 2022). However, the adjusted V_d in estimating the aerosol
197 was too coarse. In Eq. (3), the parameterizations of R_a and R_b determined the magnitude of V_d . P22 dry
198 deposition scheme in CMAQv5.4 includes the white-cap effect over the ocean surface, which is related
199 to the particle collection efficiency by impaction, as a function of R_b (Pleim et al., 2022). The impact of
200 the white cap can increase as the wind speed increases, which can be an essential parameterization in
201 simulating transboundary events (Albert et al., 2020). Our findings on dust transport, which was highly
202 related to turbulence, have significant implications for future research and modeling, inspiring further
203 exploration and innovation (Zhang et al., 2022). In CMAQv5.4, R_b is estimated separately by vegetation
204 and non-vegetation type. R_b at the smooth surface (non-vegetation) is related to the surface resistivity of
205 the bare soil and the water layer. Since EAD aerosol particles are mostly uplifted from the bare soil surface
206 layer and the aerosol deposition at the marine boundary layer (Kong et al., 2021), the sensitivity of R_b at
207 the smooth surface impact on the CMAQ dust model simulation can be vital. By assuming $R_b = 1/V_d$, V_d
208 is inversely dependent on R_b , we increased R_b to a factor of 10 as P22E01. To further carry out the
209 sensitivity test, we scale R_s by 50 and 100, for P22E02 and P22E03, respectively (Table 2).

210 2.4 Ancillary dataset

PM₁₀ (particulate matter $\leq 10 \mu\text{m}$ in aerodynamic diameter) and PM_{2.5} (particulate matter $\leq 2.5 \mu\text{m}$ in aerodynamic diameter) concentrations during the dust events in January 2023 were obtained from Lulin Atmospheric Background Station (LABS; 23.47° N, 120.87° E, 2862 m MSL) and Cape Fuguei (25.30° N, 121.54° E, 10 m MSL). In addition, the hourly PM₁₀ and PM_{2.5} of nearly 100 sites distributed over mainland China (Fig. S1), covering the period of 12 March-20 April 2021, obtained from the Chinese air quality online monitoring analysis platform's website (www.aqistudy.cn/). The Modern Era Retrospective-analysis for Research and Application version 2 (MERRA-2) reanalysis data was used to demonstrate the spatiotemporal distribution of dust, compare with the air quality model, irrespective of the influence of clouds. MERRA-2 (Gelaro et al., 2017) is a NASA reanalysis utilizing Goddard Earth Observing System Data Assimilation System Version 5 (GEOS-5) and covering the data assimilated system at a native spatial resolution of $0.5^\circ \times 0.625^\circ$. Also, Moderate Resolution Imaging Spectroradiometer (MODIS) Terra satellite images and the level-3 MODIS AOD at 550 nm (MYD08) were obtained from the U.S. National Aeronautics and Space Administration (<https://worldview.earthdata.nasa.gov/>).

3 Results and Discussion

3.1 Observed air quality and weather conditions

Figure 2 shows the dust outbreak over East Asia, displayed by the MODIS Terra sensor and MODIS AOD at 550 nm from 22-31 January 2023. The satellite image showed dust induced by a high-pressure system on 24-25 January (Fig. 2a3, 2a4). The next day, the same region was covered by a thick cloud, and dust was again widely distributed from 27-30 January 2023. Using MODIS AOD to verify the dust plume (Han et al., 2012; Kong et al., 2021), the dust plume was distributed in Central China and northern Taiwan on 24 January 2023. Moreover, the most intense dust plume in the eastern China and East China Sea region was observed on 27 January. Fig. S2 shows the synoptic weather map across the study domain. On 22-23 January, the southward high-pressure system was responsible for pushing the pollutant across the Asian Continent, which is consistent with Chuang et al. (2018) and Kong et al. (2021, 2022, 2024) (Fig. S1a-b). The high-pressure system that moved southward will then move eastward toward the western

237 Pacific Ocean (Fig S1c-d). Meanwhile, the high-pressure system on the northwest side again expands in
238 the southeast direction. The second high-pressure system again pushed the pollutant for the second time
239 and caused the high pollutant problem on 27 January.

240 The impact of East Asian dust on the air quality over the high-altitude western Pacific region was
241 widely discussed (Kong et al., 2022). Two interesting high pollution events at Mt. Lulin (2,862 m above
242 sea level) during 24-26 Jan and 27-30 January, respectively, are shown in Fig. 3. The latter event was
243 more intense compared to the earlier one, where the maximum PM₁₀ concentration can reach up to 35 µg
244 m⁻³. Moreover, it was observed that the BC concentrations could reach up to a maximum of 400 ng m⁻³.
245 Based on the *in-situ* measurement, it was interesting to find the mixing state between dust, BC, and brown
246 carbon (Fig. 3c). Different from what has been discussed by Kong et al. (2022), the long-range transport
247 air pollution at the high-altitude not just merely EAD, but also included the anthropogenic pollutant from
248 mainland China.

249 3.2 Evaluation of CMAQ dust emission and dry deposition parameterizations

250 Table 3 shows the statistical analysis of PM₁₀ and PM_{2.5} concentrations over Cape Fuguei (northern
251 Taiwan) from 22-31 January under the multiple deposition mechanisms. The threshold of the statistical
252 index is based on Emery (2001). CMAQ_Off_S22, the PM₁₀ simulation presented without the inline dust
253 calculation, recorded the normalized mean bias (NMB) of -52.81 %. CMAQ_Dust_S22 improved the
254 simulation over Cape Fuguei (northern Taiwan) by -47.01 % as we included the refined dust treatment
255 (Kong et al., 2024). However, the improvement is insignificant due to the weak intensity dust episodes
256 and the limitation due to the excessive deposition mechanism within the model (Kong et al., 2021). Hence,
257 we expanded the sensitivity simulation to examine the impact of the deposition algorithm on the aerosol
258 prediction. CMAQ_Dust_E20 simulations utilizing the Emerson et al. (2020) approach increased the
259 modeled PM₁₀ simulation by NMB of -41.9 %.

260 Instead of PM₁₀ simulation, the present study found that the inline dust treatment and deposition
261 algorithms could influence PM_{2.5} simulation performances. For instance, the modeled PM_{2.5} improved
262 from -12.63 % (CMAQ_Off_S22) to -8.84 % (CMAQ_Dust_S22). Meanwhile, the deposition algorithm

263 embedded in CMAQv5.4 has recorded modeled $PM_{2.5}$ by -10.65 % and -15.22 % under
264 CMAQ_Dust_E20 and CMAQ_Dust_P22, respectively. This incident suggested that the East Asian dust
265 from northwest China transported to the Western Pacific Ocean could also carry the anthropogenic
266 emission of East China.

267 Figure 4 shows the time series of hourly PM_{10} and $PM_{2.5}$ concentrations over Cape Fuguei
268 (northern Taiwan) and LABS (high altitude region) from 22-31 January 2023 under the multiple
269 deposition mechanisms. Generally, all the patterns of PM_{10} simulations were consistent with the observed
270 PM_{10} , especially in capturing the peak value. For instance, the maximum observed (CMAQ_Dust_E20)
271 PM_{10} concentrations at the surface during Jan 24 and 27 were 141 (102.6) $\mu g\ m^{-3}$ and 114 (163.2) $\mu g\ m^{-3}$,
272 respectively. A similar time-series pattern was found for the $PM_{2.5}$ simulation (Fig. 4b).

273 More importantly, the CMAQ model performance over the high-altitude region needed to be
274 carried out and discussed. The biomass-burning episode of the northern PSEA over Mt. Lulin has been
275 finely correlated by plume rise injection (Chuang et al., 2016; Ooi et al., 2021). From Fig. 4c, the modeled
276 PM_{10} pattern for CMAQ_Off_S22 could not correlate well with observed PM_{10} over Mt. Lulin, with a
277 poor correlation of 0.30. The correlation was increased for CMAQ_Dust_S22 (0.54), CMAQ_Dust_P22
278 (0.46), and primarily well performed for CMAQ_Dust_E20 (0.55). The modeled result
279 was somehow consistent with the surface PM_{10} simulation at Cape Fuguei. The high observed PM_{10}
280 episodes during 27-28 January with a maximum of 34.5 $\mu g\ m^{-3}$ was only 53.3 % higher than
281 CMAQ_Dust_E20 of 22.5 $\mu g\ m^{-3}$. For the CMAQ $PM_{2.5}$, the simulation generally underestimated the
282 observed $PM_{2.5}$.

283 During the spring of 2021, a series of dust storms (15 March, 27 March, and 18 April) occurred
284 over the Gobi area, with one of the most significant dust storms in the past decade (15 March, the “3.15”
285 dust storm hereafter) causing environmental impact over the continental (Jin et al., 2022; Gui et al., 2022;
286 He et al., 2022; Liang et al., 2022; Tang et al., 2022). More interestingly, one of the multiple dust storm
287 episodes reached western Pacific Ocean due to the extreme typhoon episode (Kong et al., 2024). Hence,
288 we intend to re-emphasize the precision of various deposition schemes on the CMAQ for the recent dust

289 storm episode over the Asian Continental highlighted by Kong et al. (2024). We evaluated the CMAQ
290 simulations with the different dry deposition schemes for the 40-day sensitivity test on 12 March-20 April
291 2021 against measured PM₁₀ and PM_{2.5} concentrations across the observation sites in mainland China
292 (Table 4). The observation sites used for the model comparison are marked in Fig. S1. Generally, the
293 evaluation results for Taiwan and mainland China were consistent. During the 40 days of Spring 2021,
294 the CMAQ PM₁₀ of NMB was the highest for Off_S22 (NMB = -75.00 %), followed by Dust_S22 (-45.97
295 %). The latest inline dust emission scheme embedded with E20 dry deposition scheme for PM₁₀ was well
296 performed by NMB of -25.43 %, compared to the Dust_P22 (-59.82 %). For the PM_{2.5} simulation,
297 Dust_S22 has been improved from Off_S22, and Dust_S22 was slightly better than Dust_E20 and
298 Dust_P22.

299 Figure 5 shows the scatter plot of simulated and observed PM across mainland China. The
300 correlation coefficient (R), a factor of two (FAC2), and the mean observed and simulated PM are marked
301 in Figure 5. The modeled PM₁₀ without the dust scheme had the lowest correlation. Among all of these
302 simulations, Dust_E20 performed the best correlation (R > 0.3) compared to Dust_S22 and Dust_P22.
303 However, for PM_{2.5}, the correlation between the model and measured values was similar for all the dry
304 deposition schemes. The statistical index of FAC2 was used in the present work since either low or high
305 outliers less influence it (Chan and Hanna, 2004). The dataset is reliable for FAC2 values between 0.5
306 and 2.0, with the ideal model of 1.0. The simulated PM₁₀ by Dust_E20 performed well, with a nearly
307 perfect value of 1.1. Meanwhile, the PM_{2.5} by Dust_S22 simulation was slightly better than Dust_E20 but
308 much better than the other experiments.

309 The comparison of AOD between CMAQ and MODIS for the three dust storm episodes: 14-16
310 March 2021 (“3.15” dust storm), 26-28 March 2021 (“3.27” dust storm), and 17-19 April 2021 was shown
311 (“4.18” dust storm) (Table 4). Overall, CMAQ Dust_E20 above 30°N has evaluated well the MODIS
312 AOD by NMB of -26.2 %, as compared to S22 (-32.0 %) and P22 (-35.8 %). The CMAQ AOD by E20
313 during the most intense Super Dust Storm in 3.15 has significantly improved over northern China, the
314 dust source region, as shown in the red dash rectangular box (Fig. S3). Additionally, the modeled AOD
315 by E20 over the western Pacific Ocean (shown in red dash rectangular box) increased in episode 4.18,

316 reporting a value of 0.7 compared to 0.5 by S22. Significantly, the E20 deposition scheme has primarily
317 enhanced the PM₁₀ prediction over the marine boundary layer, addressing the model uncertainty due to
318 the typhoon mentioned by Kong et al. (2024) and demonstrating the practical implications of our research.

319 The present work is consistent with the dust scheme in the WRF-Chem, where the dust loading is
320 very sensitive to the dry deposition schemes and dust emission schemes, especially over the downwind
321 region (Zeng et al., 2020). Fig. 6 shows the CMAQ estimated averaged mean PM₁₀ and PM_{2.5} in January
322 2023 and Spring 2021 for the Off_S22 and its corresponding change by Dust_S22, Dust_E20, and
323 Dust_P22, respectively. Generally, the spatial distribution of the high PM₁₀ concentrations by > 50 µg m⁻³
324 was distributed over northwest China, which is the dust source region's location, consistent with the
325 simulation suggested by Kong et al. (2021, 2022, 2024). Such high particulate matter dissipated to east
326 China, indicating the transport pathway in the southeastern direction towards the western Pacific (Fig. 6a,
327 h). The larger PM₁₀ distribution by E20 than S22 and P22 over northwest China, meaning E20
328 successfully increased the PM₁₀ concentrations. Another fascinating fact about E20 was that the PM₁₀
329 increased over the southern South China Sea (Fig. 6b). For the modeled PM_{2.5} concentrations, the high
330 concentration was distributed over the Asian Continental under all dry deposition mechanism.

331 3.3 Impact on the CMAQ ambient particle concentrations

332 Figure 7 shows the boxplot of the averaged simulated V_d for the Aitken, accumulation, and coarse
333 particles modes under multiple deposition schemes in January 2023 (S22_2023, E20_2023, and
334 P22_2023) and in Spring 2021 (S22_2021, E20_2021, and P22_2021). These different dry deposition
335 treatments have a substantial impact on the aerosol profile, altering the ambient total dry deposition
336 regionally. For instance, the median deposition velocity of S22_2023, E20_2023, and P22_2023 of the
337 Aitken (accumulation) modes particle were 0.069 (0.020) cm s⁻¹, 0.039 (0.014) cm s⁻¹ and 0.034 (0.029)
338 cm s⁻¹, respectively. The E20 simulation median V_d decreased by -12.65 % for coarse-mode particles
339 compared to S22. Also, the 75th percentile V_d of the coarse mode has been significantly reduced by -32.13
340 %. On the other hand, P22 showed a different simulation by the median V_d increment of 71.38 %. These
341 findings suggest that the choice of dry deposition treatment can significantly influence the distribution
342 and concentration of aerosols in the atmosphere, with potential implications for air quality and climate.

As shown in Figure 7, the results during the spring of 2021 are similar to those for the 2023 results for the median deposition velocity. For instance, the V_d Aitken, accumulation and coarse mode for E20_2023 (E20_2021) were 0.039 (0.039) cm s^{-1} , 0.014 (0.012) cm s^{-1} and 0.20 (0.19) cm s^{-1} , respectively. The result was consistent with the best simulated PM_{10} by E20 in 2023 and 2021 displayed in Table 3 and 4, respectively. The lowest V_d of the coarse mode particle was responsible for reducing the PM_{10} simulation underestimation of S22 and P22, consistent with the simulation by Ryu and Min (2022). The slow V_d means the total loss of aerosol to the surface has been minimized, leading to increased aerosol concentration. These implications are crucial for understanding the behaviour of aerosols in the atmosphere and their impact on air quality.

We estimated the CMAQ averaged particle modes for the S22_2023, E20_2023, and P22_2023 dry deposition scheme (Fig. 8). For S22_2023, we found that high V_d corresponding to the Aitken and accumulation modes distributed mainly over most of the CMAQ domain, which was most evident over Asian continent (Fig 8a, 8d). Meanwhile, the magnitude of V_d distribution was the most significant over the western Pacific Ocean by S22_2023 and the least for E20_2023 (dash rectangular box in Fig. 8d, e, f). For the coarse mode particles, the V_d was the lowest for E20_2023 compared to S22_2023 and P22_2023, particularly over the ocean area near northeast China, Japan, and Korea (white-dash rectangular box in Fig. 8d, e, f). This leads to a significant deposition over the downwind region, causing less PM_{10} simulated by P22_2023 and S22_2023 than E20_2023. A previous study proposed the V_d for the aerosol at the water surface was associated with the CTM uncertainly at the downwind region (Kong et al., 2021, 2024; Ryu and Min, 2022). The V_d at land surface was generally higher than at water surfaces. Interestingly, the coarse mode V_d at the water surface for E20_2023 (0.060 cm s^{-1}) was lower than S22_2023 (0.085 cm s^{-1}) and P22_2023 (0.116 cm s^{-1}), respectively, suggesting that E20_2023 deposition schemes could minimize the excessive deposition over the marine boundary layer (Table 5). Such minimal deposition velocity distributing over a large part of the western Pacific Ocean, including the Sea of Japan, Yellow Sea, East China Sea, and South China Sea, might be responsible for reducing the modeled PM_{10} underestimation over Taiwan (Fig. 8h), as mentioned by Kong et al. (2021).

To better understand the behavior of the V_d during the 40-day simulation of Spring 2021 corresponding to the aerosol simulation, we visualized the CMAQ averaged particle modes for the S22_2023, E20_2023, and P22_2023 dry deposition scheme (Fig. 9). The V_d of the coarse mode particles for E20_2021 was the lowest among the others over the ocean area, which shows similarity as E20_2023 (Fig. 9g, h, i). As mentioned by Kong et al. (2024), one of the continuous EAD episodes was related to the typhoon. The strong wind speed and extreme precipitation due to the intense anticyclonic system caused nearly zero dust simulation. In S22_2021 (0.060 cm s^{-1}) and P22_2021 (0.070 cm s^{-1}), the model suggested high coarse mode V_d at the western Pacific Ocean. In E20_2021, the V_d (0.053 cm s^{-1}) is lower than the rest of the dry deposition mechanism, particularly the area affected by typhoon (black-dash rectangular box). This means that the E20 dry deposition has reduced the uncertainty of the excessive dust loss at the marine boundary layer. Figure 6 (g, h, i) shows more simulated mineral dust at the western Pacific by E20 than S22 and P22 during the spring of 2021.

3.4 CMAQ of dust and black carbon synoptic pattern at the upper level

Black carbon (BC), often known as elemental carbon, released from the biofuels, fossil fuels and biomass burning, has been proven to impact the radiative budget and regional climate (Ramanathan, V and Carmichael, 2008; Pani et al., 2016, 2020). In the meantime, China has been a significant contributor to global anthropogenic BC emission, particularly in the cities of the northern part (Xiao et al., 2023; Wang et al., 2024). During the severe dust episodes in the spring of 2023, the contribution of black carbon brought by EAD was captured in North China (Wang et al., 2024). As depicted in Fig. 2, the transboundary episode observed in the upper level of Taiwan during this event could be the mixing of the natural dust and anthropogenic haze episodes, which demonstrates the consistency. Additionally, blending mineral dust with anthropogenic transport due to the north easterly wind, a wind that blows from the northeast, has been a subject of extensive discussion (Lin et al., 2007, 2012; Li et al., 2012). During the EAD, the dust from the Gobi Desert that was transported towards the western Pacific region could also carry anthropogenic aerosol, contributing to different levels of pollutant concentration. However, the distinct transport pathway at the high altitude between both aerosol types is a topic that has received less attention but is of significant importance to our understanding of atmospheric dynamics.

396 Figure 10 illustrates mineral dust and BC concentration's spatial and temporal distribution under
397 the CMAQ_Dust_E20 scenario at 700 hPa from 24-31 January. The model reveals a high proportion of
398 modeled dust aerosol (red dash circle) at the source region, indicating an uplift from the surface to 700
399 hPa (Fig. 10a). This uplift, driven by the strong pressure gradient at the surface and the 'eastward moving
400 trough system' at the upper level (700 hPa), is a key factor in the eastward and southward transfer of the
401 dust (Fig. 10b). The high dust fraction reappears at the source region (Fig. 10c) and is transported
402 eastwardly by the similar upper-level trough (Fig. 10d), causing a long dust belt at 15°N, distributing over
403 central Asia continental, Taiwan Straits, Taiwan and large part of western Pacific Ocean. (Fig. 10e). On
404 29 January, the model of E20 clearly predicted that the dust plume moved in the southward direction
405 toward the South China Sea (Fig. 10f). The dust aerosol was left distributed at a certain part of the northern
406 South China Sea and the Philippine Sea until it totally dissipated (Fig. 10g, h). This interesting result
407 suggests the possible EAD at the longer distance at the upper level, which is a topic for further
408 investigation.

409 The southward high-pressure system responsible for the long-range transport haze episode has
410 been widely discussed (Chuang et al., 2008; Kong et al., 2021)—however, the upper-level transboundary
411 transport needs to be addressed more. While focusing on CMAQ_Dust_E20, we attempted to characterize
412 the long-range transport of modeled black carbon at the upper level (700 hPa) (Fig. 10i-p). As shown in
413 Fig. 10(i), the modeled black carbon concentration is shown to be significantly distributed at central
414 China. The black carbon transport pattern followed the eastward-moving trough system as the plume
415 moved eastward and southward (Fig. 10m, n). Interestingly, the long black carbon belt is consistent with
416 the long dust belt, as shown in Fig. 10(e, f). For instance, both modeled dust and BC were distributed at
417 the western Pacific Ocean (Fig. 10e, f, m, n) and South China Sea (Fig. 10g, o). This means that the BC
418 due to the anthropogenic emission and the natural EAD shared a similar transport pattern at the upper
419 level, driven by the trough system. Such consistency has been verified by the MERRA-2 dust and BC
420 mass column over the region (red dash rectangular in Fig. S5).

421 The dust aerosol vertical profiles (Fig. 11) show a significant distribution of the large dust fraction
422 over the Asian Continent under all simulation scenarios (Fig. 11a1-e1), as indicated by the transect drawn

423 in Fig. 1. The westerly winds, depicted in Fig. 10, facilitated the eastward transport of the aerosol plume
424 towards the western Pacific Ocean, where it accumulated along the 700 hPa altitude. Another plume was
425 observed across the ocean on the east side of Taiwan Island (Fig. 11b1). On 27 January, showed another
426 substantial fraction of dust covering the Asian Continent and Western Pacific Ocean, with significantly
427 higher dust concentrations compared to Fig. 11a1. The plume distributed eastward exhibited a clear dust
428 dome (Fig. 11a5-e5). These findings have important implications for understanding and predicting dust
429 aerosol transport patterns and their potential environmental impact.

430 The vertical profile of the modeled BC mirrors the transport pattern of mineral dust, as shown in
431 Fig. 12. A transparent BC dome was distributed along 700 hPa, echoing the pattern observed for dust.
432 This simulation suggests the consistency of the “double dome” mechanism of Asian dust and biomass
433 burning episodes (Dong et al., 2018; Huang et al., 2019). The potential warming effect of such a
434 mechanism is a topic ripe for future studies. However, it's important to note that the dust dome contains
435 a higher fraction of concentrations than the black carbon dome. The present simulation suggests that dust
436 aerosol can reach up to 500 hPa, which is consistent with Kong et al. (2021). On the other hand, the black
437 carbon plume was slightly lower, with approximately 600 hPa of the maximum height under the same
438 meteorological condition. This section, which discusses the similarity and distinctiveness of natural dust
439 and anthropogenic aerosol at the upper level, highlights the need for further study. The present simulation
440 did not consider the two-way coupling model, and it is strongly suggested for future research.

441 Table 6 shows the modeled deposition and mass concentration for different simulation scenarios
442 in January 2023. The simulation of the wet deposition and mass concentration for dust aerosol was the
443 highest by E20. This is consistent with the globally averaged aerosol number concentrations over the
444 ocean for the large size particle (Emerson et al., 2020). Contrary, P22 was the lowest in simulated wet
445 deposition and mass concentration. P22 could increase the accumulation mode's V_d and reduce the $PM_{2.5}$
446 over CONUS, which is similar to the present result (Pleim et al., 2022). Moreover, the present simulation
447 by P22 showed the highest V_d of the coarse mode that leads to the less simulated PM_{10} . P22 revised the
448 impaction collective efficiency, which is the parameterization of R_b . In order to understand the sensitivity
449 of R_b on CMAQ simulation, the R_b has been scaled up, as shown in Table 2. Generally, the increment of

450 R_b has gradually increased the wet deposition (surface mass concentration) by 13.6 (45.8) %, 25.2 (83.3)
451 %, and 28.2 (93.7) %, under P22E01, P22E02 and P22E03, respectively. In addition, the increment
452 intensity at the surface was higher than at the upper level. The simulated dust at western Pacific Ocean
453 responding to the different dry deposition schemes was shown during 27 January in Figure 11 (red-dash
454 rectangular box). As R_b increased by P22E01 and P22E03, the simulated PM_{10} by base scheme P22 (~ 30
455 $\mu g m^{-3}$), has increased to $\sim 40 \mu g m^{-3}$ and $\sim 50 \mu g m^{-3}$, respectively. It is worth noted that P22E03 simulated
456 a similar dust concentration as E20, indicating the importance of revising the R_b . On the contrary, the wet
457 deposition and mass concentration were most significant for modeled BC under the S22 dry deposition
458 scheme (Table 6). P22E01 only showed a minor increment, but it was nearly identical for P22E02 and
459 P22E03 compared to P22.

460 **4.0 Summary and Conclusions**

461 The chemical transport model is considered sensitive to the dry deposition parameterization besides the
462 dust emission treatment. The present study demonstrates the impact of the dry deposition
463 parameterizations (S22, E20, and P22) on aerosol performance in East Asia. It provides a significant
464 analysis of the transboundary transport of East Asian Dust to Taiwan from a 22-31 January 2023 case
465 study and multiple heavy dust storm episodes from 12 Mar-20 Apr 2021. Incorporating the latest dust
466 emission treatment (Kong et al., 2024) into the CMAQ slightly improved the model performance to -
467 47.01 % from -52.81 %. By implementing the E20 dry deposition scheme, characterized by calibrating
468 the collection efficiency by Brownian diffusion and interception, the CMAQ simulation of the surface
469 PM_{10} has been improved by NMB of -41.9 %, as compared to the dry deposition proposed by P22 (-53.90
470 %). Moreover, the modeled PM_{10} pattern by E20 at the upper level (700 hPa) was mainly consistent with
471 the observed PM_{10} , especially in capturing the peak value. The dry deposition of E20 was correlated well
472 with the high altitude in situ by 0.55, as compared to S22 (0.54) and P22 (0.46). On the contrary, simulated
473 surface $PM_{2.5}$ by S22 has been improved to -8.84 % from -12.63 % after using the latest dust treatment,
474 and slightly better performance than E20 (-10.65 %) and P22 (-15.22 %). Additionally, the simulations
475 of the multiple dust episodes in spring 2021 were re-constructed to evaluate the CMAQ performance over
476 the Asian Continental. The E20 dry deposition scheme outperformed the others with the lowest NMB

477 value in simulating PM_{10} (-25.4 %) and AOD (-26.2%). For the modeled $PM_{2.5}$, S22 performed slightly
478 better than E20, with NMB of -36.29 % and -37.5 %, respectively.

479

480 The previous CMAQ model, modulated by Kong et al. (2021; 2024), showed excessive deposition at the
481 marine boundary layer, leading to underestimating the modeled surface PM_{10} . However, using the E20
482 scheme over the entire model domain, our updated model has the lowest V_d . This precise reduction of V_d
483 of the coarse mode particle, responsible for reducing the PM_{10} simulation underestimation, has not just
484 minimized, but effectively minimized the total loss of aerosol to the surface, leading to a concentration
485 increment. Furthermore, the low-lying modeled V_d across the water surface by E20 could be crucial in
486 reducing the excessive aerosol deposition over the ocean layer.

487

488 It is worth revealing that the transboundary transport of EAD from the Asian continent towards the
489 western Pacific Ocean at the upper level was associated with the eastward moving trough system. Such
490 transport mechanisms have been found to bring along black carbon aerosol, which is primarily the main
491 element of China's human-made emissions. More interestingly, both aerosol profiles created a "long dust-
492 black carbon belt" along the 15°N. The 'double dome mechanism', a concept proposed by Huang et al.
493 (2019) that depicts the superposition of the two aerosol types, was also simulated in the present study.
494 Besides the similarity of both, the discrepancy in the case of the aerosol deposition and mass concentration
495 was shown. By comparing the base P22 scheme to the revised scheme (P22E01-P22E03), wet deposition
496 increases and hence increases the dust aerosol. In other ways, black carbon aerosol also increases in a
497 minimal magnitude, not as much as dust aerosol. This study highlights the importance of dry deposition
498 schemes for the modeled dust and black carbon concentration and provides a reference for better dry
499 deposition schemes in CTMs over East Asia.

500 Data Availability

501 MERRA-2 data are available online through the NASA Goddard Earth Sciences Data Information
502 Services Center (GES DISC; <https://disc.gsfc.nasa.gov>; last access: 01 August 2024). MODIS data used

503 in this study are available at <https://asdc.larc.nasa.gov/>(last access: 01 August 2024). The observational
504 data at LABS can be ordered by contacting corresponding authors.

505 **Author Contribution**

506 **Steven Soon-Kai Kong:** Conceptualization; Data curation; Formal analysis; Investigation; Methodology;
507 Software; Validation; Visualization; Writing – original draft; Writing – review and editing.

508 **Joshua S. Fu:** Conceptualization; Investigation; Methodology; Formal analysis; Writing – review and
509 editing.

510 **Neng-Huei Lin:** Conceptualization; Visualization; Supervision; Funding acquisition; Resources; Writing
511 – review and editing.

512 **Guey-Rong Sheu:** Funding acquisition; Resources.

513 **Wei-Syun Huang:** Data curation; Software.

514 **Competing Interests**

515 Some authors are members of the editorial board of journal ACP.

516 **Acknowledgments**

517 We acknowledged the National Science and Technology Council of Taiwan, under Project No.
518 NSTC113-2811-M-008-045 for supporting the research. We also acknowledged the staff at LABS, and
519 EPA Taiwan for the provision of the ground-based measurement datasets. We are also thankful to
520 MERRA-2 and MODIS for the satellite product.

521 **References:**

522 Albert, M. F., Anguelova, M. D., Manders, A. M., Schaap, M., & Leeuw, G. D.: Parameterization of
523 oceanic whitecap fraction based on satellite observations. *Atmospheric Chemistry and Physics*, 16, 21,
524 13725–13751. <https://doi.org/10.5194/acp-16-13725-2016>, 2016.

525 Chang, J. and Hanna, S.: Air quality model performance evaluation, *Meteorol Atmos Phys.*, 87, 167–196,
526 <https://doi.org/10.1007/s00703-003-0070-7>, 2004.

527 Chuang, M. T, Fu, J. S., Lee, C., Lin, N., Gao, Y., Wang, S., Sheu, G., Hsiao, T., Wang, J., Yen, M., Lin,
528 T., and Thongboonchoo, N.: The Simulation of Long-Range Transport of Biomass Burning Plume and
529 Short-Range Transport of Anthropogenic Pollutants to a Mountain Observatory in East Asia during the
530 7-SEAS / 2010 Dongsha Experiment, 2933–2949, <https://doi.org/10.4209/aaqr.2015.07.0440>, 2016.

531 Chuang, M. T., Fu, J. S., Jang, C. J., Chan, C. C., Ni, P. C., and Lee, C. Te: Simulation of long-range
532 transport aerosols from the Asian Continent to Taiwan by a Southward Asian high-pressure system, *Sci.*
533 *Total Environ.*, 406, 168–179, <https://doi.org/10.1016/j.scitotenv.2008.07.003>, 2008.

534 Chuang, M.-T., Ooi, M. C. G., Lin, N.-H., Fu, J. S., Lee, C.-T., Wang, S.-H., Yen, M.-C., Kong, S. S.-K.,
535 and Huang, W.-S.: Study on the impact of three Asian industrial regions on PM_{2.5} in Taiwan and the
536 process analysis during transport, *Atmos. Chem. Phys.*, 20, 14947–14967, [https://doi.org/10.5194/acp-](https://doi.org/10.5194/acp-20-14947-2020)
537 [20-14947-2020](https://doi.org/10.5194/acp-20-14947-2020), 2020.

538 Dong, X., Fu, J. S., Huang, K., Tong, D., and Zhuang, G.: Model development of dust emission and
539 heterogeneous chemistry within the Community Multiscale Air Quality modeling system and its
540 application over East Asia, *Atmos. Chem. Phys.*, 16, 8157–8180, [https://doi.org/10.5194/acp-16-8157-](https://doi.org/10.5194/acp-16-8157-2016)
541 [2016](https://doi.org/10.5194/acp-16-8157-2016), 2016.

542 Dong, X., Fu, J. S., Huang, K., Lin, N., Wang, S., and Yang, C.: Analysis of the Co-existence of Long-
543 range Transport Biomass Burning and Dust in the Subtropical West Pacific Region, *Sci. Rep.*, 1–10,
544 <https://doi.org/10.1038/s41598-018-27129-2>, 2018.

545 Dong, X., Fu, J. S., Huang, K., Zhu, Q., and Tipton, M.: Regional climate effects of biomass burning and
546 dust in East Asia: Evidence from modeling and observation, *Geophysical Research Letters*, 46,
547 <https://doi.org/10.1029/2019GL083894>, 2019.

548 Emerson, E. W., Hodshire, A. L., DeBolt, H. M., Bilsback, K. R., Pierce, J. R., McMeeking, G. R., and
549 Farmer, D. K.: Revisiting particle dry deposition and its role in radiative effect estimates, *Proc. Natl.*
550 *Acad. Sci. U. S. A.*, 117, 26076–26082, <https://doi.org/10.1073/pnas.2014761117>, 2020.

551 Foroutan, H., Young, J., Napelenok, S., Ran, L., Appel, K., Gilliam, R., and Pleim, J.: Journal of Advances
552 in Modeling Earth Systems, J. Adv. Model. Earth Syst., 9, 585–606,
553 <https://doi.org/10.1002/2013MS000282>. Received, 2017.

554 Gaydos, T. M., Pinder, R., Koo, B., Fahey, K. M., Yarwood, G., and Pandis, S. N.: Development and
555 application of a three-dimensional aerosol chemical transport model, PMCAMx, Atmos. Environ., 41,
556 2594–2611, <https://doi.org/10.1016/j.atmosenv.2006.11.034>, 2007.

557 Gelaro, R., McCarty, W., Suárez, M. J., Todling, R., Molod, A., Takacs, L., Randles, C. A., Darmenov,
558 A., Bosilovich, M. G., Reichle, R., Wargan, K., Coy, L., Cullather, R., Draper, C., Akella, S., Buchard,
559 V., Conaty, A., da Silva, A. M., Gu, W., Kim, G. K., Koster, R., Lucchesi, R., Merkova, D., Nielsen, J.
560 E., Partyka, G., Pawson, S., Putman, W., Rienecker, M., Schubert, S. D., Sienkiewicz, M., and Zhao, B.:
561 The modern-era retrospective analysis for research and applications, version 2 (MERRA-2), J. Clim., 30,
562 5419–5454, <https://doi.org/10.1175/JCLI-D-16-0758.1>, 2017.

563 Giardina, M. and Buffa, P.: A new approach for modeling dry deposition velocity of particles, Atmos.
564 Environ., 180, 11–22, <https://doi.org/10.1016/j.atmosenv.2018.02.038>, 2018.

565 Gui, K., Yao, W., Che, H., An, L., Zheng, Y., Li, L., Zhao, H., Zhang, L., Zhong, J., Wang, Y., and Zhang,
566 X.: Record-breaking dust loading during two mega dust storm events over northern China in March 2021:
567 aerosol optical and radiative properties and meteorological drivers, Atmos. Chem. Phys., 22, 7905–7932,
568 <https://doi.org/10.5194/acp-22-7905-2022>, 2022.

569 Han, X., Ge, C., Tao, J., Zhang, M., and Zhang, R.: Air quality modeling for a strong dust event in East
570 Asia in March 2010, Aerosol Air Qual. Res., 12, 615–628, <https://doi.org/10.4209/aaqr.2011.11.0191>,
571 2012.

572 He, Y., Yi, F., Yin, Z., Liu, F., Yi, Y., and Zhou, J.: Mega Asian dust event over China on 27–31 March
573 2021 observed with space-borne instruments and ground-based polarization lidar, Atmos. Environ., 285,
574 119238, <https://doi.org/10.1016/j.atmosenv.2022.119238>, 2022.

575 Hogrefe, C., Bash, J. O., Pleim, J. E., Schwede, D. B., Gilliam, R. C., Foley, K. M., Appel, K. W., and
576 Mathur, R.: An analysis of CMAQ gas-phase dry deposition over North America through grid-scale and
577 land-use-specific diagnostics in the context of AQMEII4, Atmos. Chem. Phys., 23, 8119–8147,
578 <https://doi.org/10.5194/acp-23-8119-2023>, 2023.

579 Huang, H.-Y., Wang, S.-H., Huang, W.-X., Lin, N.-H., Chuang, M.-T., da Silva, A. M., Peng, C.-M.:
580 Influence of synoptic-dynamic meteorology on the long-range transport of Indochina biomass burning
581 aerosols, *J. Geophys. Res.*, 111, 125, e2019JD031260. [https://doi.org/ 10.1029/2019JD031260](https://doi.org/10.1029/2019JD031260), 2020.

582 Huang, K., Fu, J. S., Lin, N.-H., Wang, S.-H., Dong, X., Wang, G.: Superposition of Gobi Dust and
583 Southeast Asian Biomass Burning: The Effect of Multisource Long - Range Transport on Aerosol Optical
584 Properties and Regional Meteorology Modification, *J. Geophys. Res.*, 124, 16, 9464-9483,
585 <https://doi.org/10.1029/2018JD030241>, 2019.

586 Huang, W. S., Griffith, S. M., Lin, Y. C., Chen, Y. C., Lee, C. Te, Chou, C. C. K., Chuang, M. T., Wang,
587 S. H., and Lin, N. H.: Satellite-based emission inventory adjustments improve simulations of long-range
588 transport events, *Aerosol Air Qual. Res.*, 21, 1–16, <https://doi.org/10.4209/AAQR.210121>, 2021.

589 Jin, J., Pang, M., Segers, A., Han, W., Fang, L., Li, B., Feng, H., Lin, H. X., and Liao, H.: Inverse
590 modeling of the 2021 spring super dust storms in East Asia, *Atmos. Chem. Phys.*, 22, 6393–6410,
591 <https://doi.org/10.5194/acp-22-6393-2022>, 2022.

592 Khan, T. R. and Perlinger, J. A.: Evaluation of five dry particle deposition parameterizations for
593 incorporation into atmospheric transport models, *Geosci. Model Dev.*, 10, 3861–3888,
594 <https://doi.org/10.5194/gmd-10-3861-2017>, 2017.

595 Kok, J. F., Parteli, E. J. R., Michaels, T. I., Karam, D. B., and Pierre, U.: The physics of wind-blown sand
596 and dust, 1–119, n.d.

597 Kong, S. S.-K., Pani, S. K., Griffith, S. M., Ou-Yang, C.-F., Babu, S. R., Chuang, M.-T., Ooi, M. C. G.,
598 Huang, W.-S., Sheu, G.-R., and Lin, N.-H.: Distinct transport mechanisms of East Asian dust and the
599 impact on downwind marine and atmospheric environments, *Sci. Total Environ.*, 827, 154255,
600 <https://doi.org/10.1016/j.scitotenv.2022.154255>, 2022.

601 Kong, S. S., Fu, J. S., Dong, X., Chuang, M., Chel, M., Ooi, G., Huang, W., Griffith, S. M., Kumar, S.,
602 and Lin, N.: Sensitivity analysis of the dust emission treatment in CMAQv5. 2. 1 and its application to
603 long-range transport over East Asia, *Atmos. Environ.*, 118441,
604 <https://doi.org/10.1016/j.atmosenv.2021.118441>, 2021.

605 Kong, S. S. K., Ravindra Babu, S., Wang, S. H., Griffith, S. M., Chang, J. H. W., Chuang, M. T., Sheu,
606 G. R., and Lin, N. H.: Expanding the simulation of East Asian super dust storms: physical transport

607 mechanisms impacting the western Pacific, *Atmos. Chem. Phys.*, 24, 1041–1058,
608 <https://doi.org/10.5194/acp-24-1041-2024>, 2024.

609 Li, M., Zhang, Q., Kurokawa, J.-I., Woo, J.-H., He, K., Lu, Z., Ohara, T., Song, Y., Streets, D. G.,
610 Carmichael, G. R., Cheng, Y., Hong, C., Huo, H., Jiang, X., Kang, S., Liu, F., Su, H., and Zheng, B.:
611 MIX: a mosaic Asian anthropogenic emission inventory under the international collaboration framework
612 of the MICS-Asia and HTAP, *Atmos. Chem. Phys.*, 17, 935–963, [https://doi.org/10.5194/acp-17-935-](https://doi.org/10.5194/acp-17-935-2017)
613 2017, 2017.

614 Liang, L., Han, Z., Li, J., Xia, X., Sun, Y., Liao, H., Liu, R., and Liang, M.: Science of the Total
615 Environment Emission, transport, deposition, chemical and radiative impacts of mineral dust during
616 severe dust storm periods in March 2021 over East Asia, *Sci. Total Environ.*, 852, 158459,
617 <https://doi.org/10.1016/j.scitotenv.2022.158459>, 2022.

618 Liu, S., Xing, J., Sahu, S. K., Liu, X., Liu, S., Jiang, Y., Zhang, H., Li, S., Ding, D., Chang, X., and Wang,
619 S.: Wind-blown dust and its impacts on particulate matter pollution in Northern China: Current and future
620 scenarios, *Environ. Res. Lett.*, 16, 114041, <https://doi.org/10.1088/1748-9326/ac31ec>, 2021.

621 Massad, R. S., Nemitz, E., and Sutton, M. A.: Review and parameterisation of bi-directional ammonia
622 exchange between vegetation and the atmosphere, *Atmos. Chem. Phys.*, 10, 10359–10386,
623 <https://doi.org/10.5194/acp-10-10359-2010>, 2010.

624 Nemitz, E., Milford, C., and Sutton, M. A.: A two-layer canopy compensation point model for describing
625 bi-directional biosphere-atmosphere exchange of ammonia, *Q. J. R. Meteorol. Soc.*, 127, 815–833,
626 <https://doi.org/10.1256/smsqj.57305>, 2001.

627 Ooi, M., Chuang, M.-T., Fu, J., Kong, S., Huang, W.-S., Wang, S.-H., Chan, A., Pani, S., and Lin, N.-H.:
628 Improving prediction of trans-boundary biomass burning plume dispersion: from northern peninsular
629 Southeast Asia to downwind western north Pacific Ocean, *Atmos. Chem. Phys.*, 20, 14947–14967,
630 <https://doi.org/10.5194/acp-2020-1283>, 2021.

631 Pani, S. K., Wang, S. H., Lin, N. H., Lee, C. Te, Tsay, S. C., Holben, B. N., Janjai, S., Hsiao, T. C.,
632 Chuang, M. T., and Chantara, S.: Radiative effect of springtime biomass-burning aerosols over northern
633 indochina during 7-SEAS/BASELInE 2013 campaign, *Aerosol Air Qual. Res.*, 16, 2802–2817,
634 <https://doi.org/10.4209/aaqr.2016.03.0130>, 2016.

635 Pani, S. K., Wang, S. H., Lin, N. H., Chantara, S., Lee, C. Te, and Thepnuan, D.: Black carbon over an
 636 urban atmosphere in northern peninsular Southeast Asia: Characteristics, source apportionment, and
 637 associated health risks, *Environ. Pollut.*, 259, 113871, <https://doi.org/10.1016/j.envpol.2019.113871>,
 638 2020.

639 Ramanathan, V and Carmichael, G.: Climate change due to BC, *Nat. Geosci.*, 1, 221–227, 2008.

640 Ravindra Babu, S., Ou-Yang, C. F., Griffith, S. M., Pani, S. K., Kong, S. S. K., and Lin, N. H.: Transport
 641 pathways of carbon monoxide from Indonesian fire pollution to a subtropical high-Altitude mountain site
 642 in the western North Pacific, *Atmos. Chem. Phys.*, 23, 4727–4740, [https://doi.org/10.5194/acp-23-4727-](https://doi.org/10.5194/acp-23-4727-2023)
 643 2023, 2023.

644 Ryu, Y. H. and Min, S. K.: Improving Wet and Dry Deposition of Aerosols in WRF-Chem: Updates to
 645 Below-Cloud Scavenging and Coarse-Particle Dry Deposition, *J. Adv. Model. Earth Syst.*, 14,
 646 <https://doi.org/10.1029/2021MS002792>, 2022.

647 Saylor, R. D., Baker, B. D., Lee, P., Tong, D., Pan, L., and Hicks, B. B.: The particle dry deposition
 648 component of total deposition from air quality models: right, wrong or uncertain?, *Tellus, Ser. B Chem.*
 649 *Phys. Meteorol.*, 71, 1–22, <https://doi.org/10.1080/16000889.2018.1550324>, 2019.

650 Shu, Q., Koo, B., Yarwood, G., and Henderson, B. H.: Strong influence of deposition and vertical mixing
 651 on secondary organic aerosol concentrations in CMAQ and CAMx, *Atmos. Environ.*, 171, 317–329,
 652 <https://doi.org/10.1016/j.atmosenv.2017.10.035>, 2017.

653 Slinn, W. G. N.: Predictions for particle deposition to vegetative canopies, *Atmos. Environ.*, 16, 1785–
 654 1794, [https://doi.org/10.1016/0004-6981\(82\)90271-2](https://doi.org/10.1016/0004-6981(82)90271-2), 1982.

655 Tang, W., Dai, T., Cheng, Y., Wang, S., and Liu, Y.: A Study of a Severe Spring Dust Event in 2021 over
 656 East Asia with WRF-Chem and Multiple Platforms of Observations, *Remote Sens.*, 14, 3795,
 657 <https://doi.org/10.3390/rs14153795>, 2022.

658 Tav, J., Masson, O., Burnet, F., Paulat, P., Bourrianne, T., Conil, S. and Pourcelot, L.: Determination of
 659 Fog-Droplet Deposition Velocity from a Simple Weighing Method. *Aerosol Air Qual. Res.* 18: 103-113.
 660 <https://doi.org/10.4209/aaqr.2016.11.0519>, 2018.

661 Wang, W., Zhou, H., Lyu, R., Shao, L., Li, W., Xing, J., Zhao, Z., Li, X., Zhou, X., and Zhang, D.:
662 Organic Carbon and Elemental Carbon in Two Dust Plumes at a Coastal City in North China, *Aerosol*
663 *Air Qual. Res.*, 24, <https://doi.org/10.4209/aaqr.240002>, 2024.

664 Wesley, M. L.: Parameterization of Surface Resistances to Gaseous Dry Deposition in Regional-Scale
665 Numerical Models, *Atmos. Environ.*, 23, 1293–1304, 1989.

666 Xiao, H. W., Xu, Y., and Xiao, H. Y.: Source apportionment of black carbon aerosols in winter across
667 China, *Atmos. Environ.*, 298, <https://doi.org/10.1016/j.atmosenv.2023.119622>, 2023.

668 Zeng, Y., Wang, M., Zhao, C., Chen, S., Liu, Z., Huang, X., and Gao, Y.: WRF-Chem v3.9 simulations
669 of the East Asian dust storm in May 2017: Modeling sensitivities to dust emission and dry deposition
670 schemes, *Geosci. Model Dev.*, 13, 2125–2147, <https://doi.org/10.5194/gmd-13-2125-2020>, 2020.

671 Zhang, L., Gong, S., Padro, J., and Barrie, L.: A size-segregated particle dry deposition scheme for an
672 atmospheric aerosol module, *Atmos. Environ.*, 35, 549–560, [https://doi.org/10.1016/S1352-](https://doi.org/10.1016/S1352-2310(00)00326-5)
673 [2310\(00\)00326-5](https://doi.org/10.1016/S1352-2310(00)00326-5), 2001.

674 Zhang, L., Zhang, H., Li, Q., Cai, X., and Song, Y.: Vertical dispersion mechanism of long-range
675 transported dust in Beijing: Effects of atmospheric turbulence, *Atmos. Res.*, 269, 106033,
676 <https://doi.org/10.1016/j.atmosres.2022.106033>, 2022.

677 Zheng, B., Tong, D., Li, M., Liu, F., Hong, C., Geng, G., Li, H., Li, X., Peng, L., Qi, J., Yan, L., Zhang,
678 Y., Zhao, H., Zheng, Y., He, K., and Zhang, Q.: Trends in China's anthropogenic emissions since 2010
679 as the consequence of clean air actions, *Atmos. Chem. Phys.*, 18, 14095–14111,
680 <https://doi.org/10.5194/acp-18-14095-2018>, 2018.

681
682
683
684
685
686
687
688
689
690
691

692 **Table 1.** Model settings.

Model setting	Descriptions
Period	12 March-20 April 2021 and 22-31 January 2023
Domain	d01, d02, and d03 with 45 KM, 15 KM, and 5 KM of the resolutions, respectively
Boundary condition	NCEP FNL lateral boundary condition
Surface and land surface model	NOAH
Numerical weather model	WRF v40, including grid and observation nudging at d01.
Chemical transport model	CMAQ v5.4
Gas-phase chemistry and aerosol mechanism	CB06e51 + AE7
Emission Inventory	MICS-ASIA III emission in 2023, adjusted from the emission in 2017 (Zhang et al., 2018) based on the OMI-NO _x satellite (Huang et al., 2021).
Online dust treatment	The refined windblown dust treatment suggested by Kong et al. (2024).
Dry deposition option	STAGE (S22, E20 and P22).

693
694 **Table 2.** Simulation scenarios used in this present study.

Experiments	Online dust emission treatment by Kong et al. (2024)	Dry deposition treatment	Surface resistance (R _b) at the smooth surface
CMAQ_Off_S22	Off	S22	Default
CMAQ_Dust_S22	On	S22	Default
CMAQ_Dust_E20	On	E20	Default
CMAQ_Dust_P22	On	P22	Default
CMAQ_Dust_P22E01	On	P22	Increased by a factor of 10
CMAQ_Dust_P22E02	On	P22	Increased by a factor of 50
CMAQ_Dust_P22E03	On	P22	Increased by a factor of 100

695
696
697
698
699
700
701
702
703
704
705
706

707 **Table 3.** Statistical evaluation for PM₁₀ and PM_{2.5} concentrations during 22-31 January 2023 for Cape
 708 Fuguei under the multiple simulation scenarios.

Benchmark		CMAQ						
		Off_	Dust_	Dust_	Dust_	Dust_	Dust_	Dust_
		S22	S22	E20	P22	P22E01	P22E02	P22E03
PM₁₀								
MeanObs		49.97	49.97	49.97	49.97	49.97	49.97	49.97
MeanMod		23.58	26.48	29.04	23.04	25.99	27.36	27.69
NMSE		0.66	0.56	0.49	0.71	0.57	0.53	0.52
NMB	± 85%	-52.81	-47.01	-41.90	-53.90	-47.99	-45.24	-44.58
R	> 0.35	0.43	0.46	0.52	0.42	0.48	0.51	0.52
NMBF		-1.12	-0.89	-0.72	-1.17	-0.92	-0.83	-0.80
PM_{2.5}								
MeanObs		15.52	15.52	15.52	15.52	15.52	15.52	15.52
MeanMod		13.56	14.15	13.86	13.16	13.26	13.22	13.20
NMSE		0.30	0.30	0.29	0.31	0.30	0.30	0.30
NMB	± 85%	-12.63	-8.84	-10.65	-15.22	-14.54	-14.80	-14.92
R	> 0.35	0.50	0.53	0.53	0.52	0.53	0.53	0.53
NMBF		-0.14	-0.20	-0.12	-0.18	-0.17	-0.17	-0.18

709 Note: the definition of the statistical formulas NMSE: Normalized Mean Square Error; NMB: Normalized
 710 Mean Bias; R: Correlation Coefficient and NMBF: Normalized Mean Bias Factor

711
 712 **Table 4.** CMAQ evaluation for PM₁₀ and PM_{2.5} against the averaged 100 observation sites across
 713 mainland China (Fig. S1) and AOD against MODIS daily observation near the dust source region (above
 714 30°N) with Normalized Mean Bias (NMB) under the multiple simulation scenarios (Fig. S3). Spring
 715 2021, 3.15, 3.27, and 4.18 represent the evaluation period by 12 March-20 April 2021, 14-16 March 2021,
 716 26-28 March 2021, and 17-19 April 2021, respectively.

Parameters	Period	CMAQ						
		Off_	Dust_	Dust_	Dust_	Dust_	Dust_	Dust_
		S22	S22	E20	P22	P22E01	P22E02	P22E03
PM ₁₀	Spring 2021	-75.00	-45.97	-25.43	-59.82	-45.09	-35.42	-32.92
PM _{2.5}	Spring 2021	-55.56	-36.29	-37.50	-42.47	-41.20	-41.51	-41.66
AOD	3.15	-80.49	-46.41	-38.97	-48.45	-44.80	-41.66	-40.80
	3.27	-80.92	-41.84	-36.39	-44.52	-41.60	-39.30	-38.72
	4.18	-83.09	-7.83	-3.20	-14.52	-9.45	-7.18	-6.67
	Mean AOD	-81.50	-32.03	-26.19	-35.83	-31.95	-29.38	-28.73

717
 718
 719
 720
 721
 722
 723
 724

725 **Table 5.** Average deposition velocity in January 2023 (S22_2023, E20_2023, and P22_2023) and Spring
 726 2021 (S22_2021, E20_2021, and P22_2021) for Aitken, Accumulation, and Coarse modes over land and
 727 ocean boundary layer, respectively.

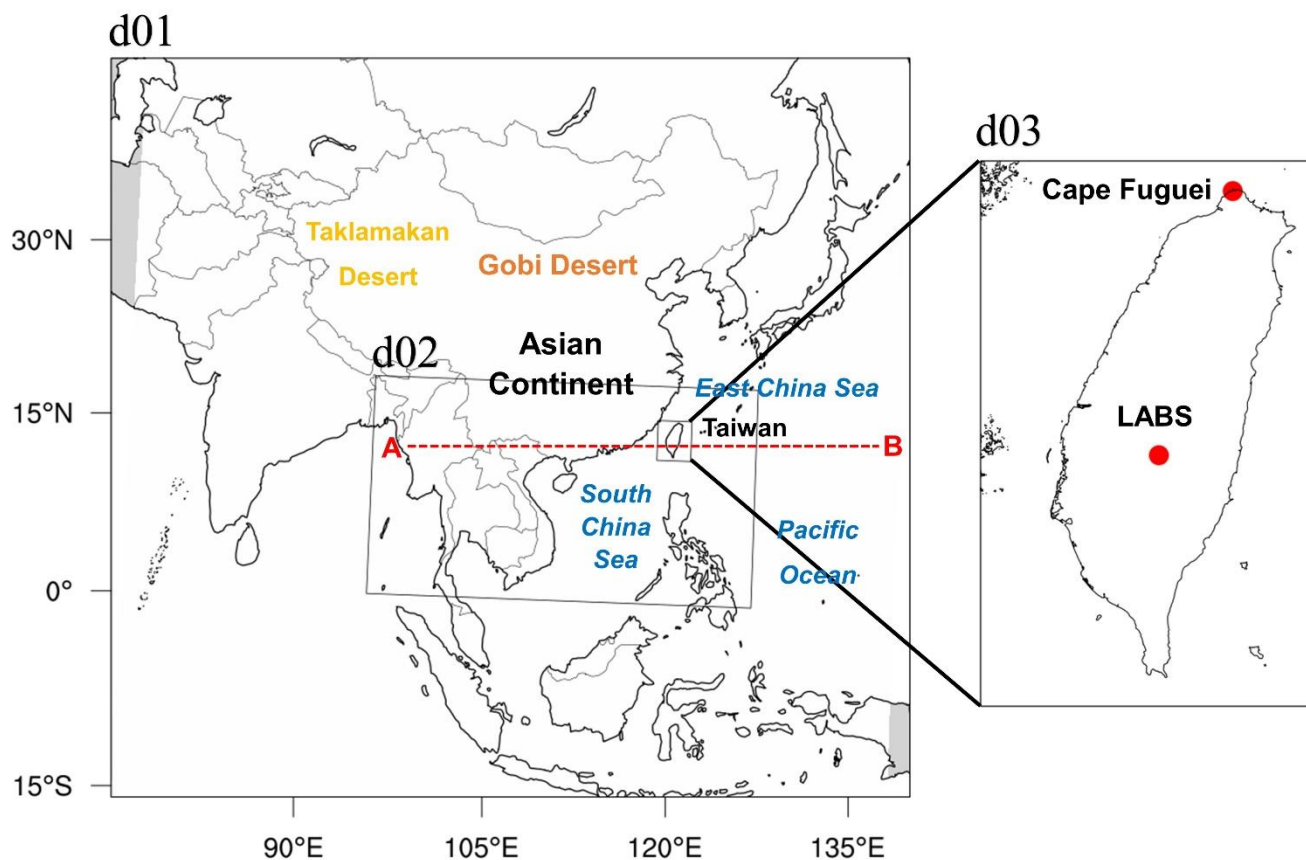
Dry deposition schemes (cm s ⁻¹)	Aitken		Accumulation		Coarse	
	Land	Ocean	Land	Ocean	Land	Ocean
S22_2023	0.219	0.117	0.120	0.064	0.078	0.085
E20_2023	0.090	0.074	0.065	0.040	0.139	0.060
P22_2023	0.085	0.062	0.072	0.043	0.290	0.116
S22_2021	0.308	0.100	0.109	0.042	0.077	0.060
E20_2021	0.139	0.063	0.063	0.026	0.142	0.053
P22_2021	0.119	0.047	0.072	0.025	0.265	0.070

728
 729
 730
 731
 732
 733
 734
 735
 736
 737
 738
 739
 740
 741
 742
 743
 744
 745
 746
 747
 748
 749
 750
 751
 752
 753

754 **Table 6.** Model averaged dry, wet deposition and mass concentration for dust and BC aerosols in January
 755 2023 (10-days averaged) for different simulation scenarios.

Dust (ASOIL)	Dry deposition (mg m ⁻²)	Wet deposition (mg m ⁻²)	Mass concentration at the surface (µg m ⁻³)	Mass concentration at 700 hPa (µg m ⁻³)
S22	0.267	0.112	6.34	3.62
E20	0.167	0.136	10.25	4.40
P22	0.300	0.103	4.79	3.56
P22E01	0.243	0.117	7.00	3.79
P22E02	0.196	0.129	8.78	4.13
P22E03	0.183	0.132	9.28	4.22
BC (AECI + AECJ)	Dry deposition (µg m ⁻²)	Wet deposition (µg m ⁻²)	Mass concentration at the surface (ng m ⁻³)	Mass concentration at 700 hPa (ng m ⁻³)
S22	5.13	50.49	492	60.04
E20	8.09	48.27	471	57.73
P22	17.79	40.96	411	50.95
P22E01	16.88	41.64	415	51.23
P22E02	16.82	41.67	415	51.27
P22E03	16.82	41.67	415	51.27

756



757

758 **Figure 1:** Modeling domain configuration in East Asia. Ground-based air quality stations in Taiwan at
 759 Cape Fuguei and Lulin Atmospheric Background Station (LABS) are shown in the zoomed panel. The
 760 red dash line (A→B) represents the transects that the aerosol plumes traveled along in this study and that
 761 are discussed in Section 3.4;

762

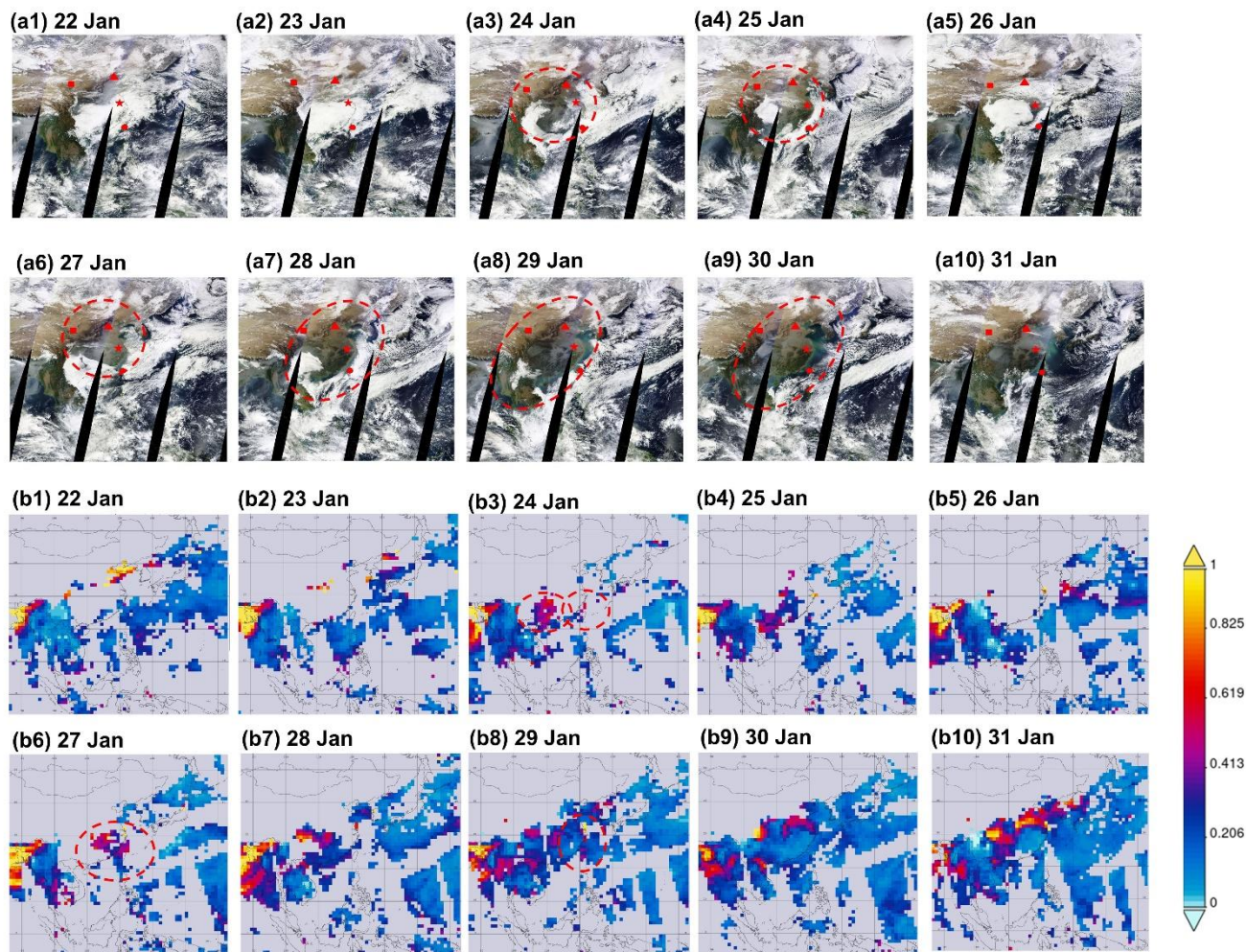
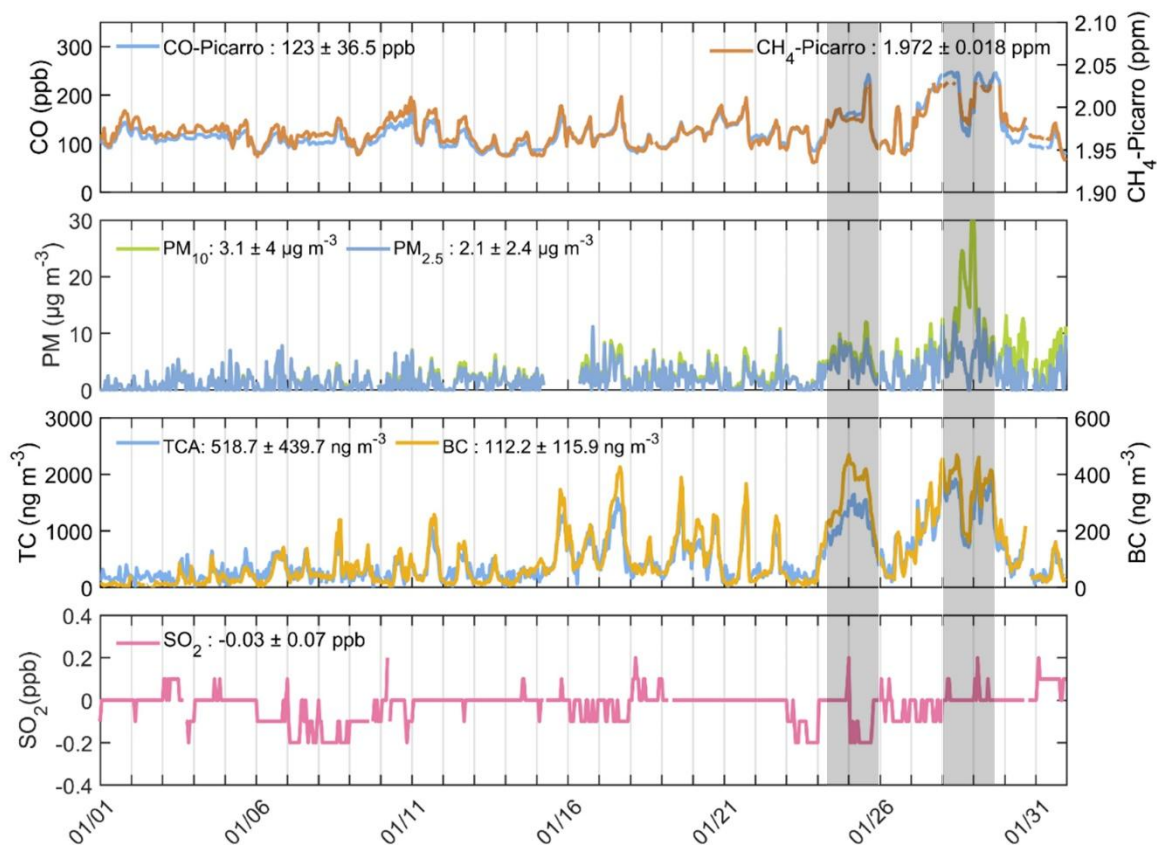
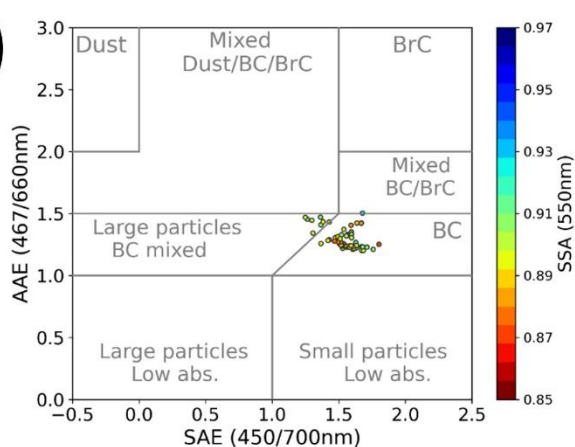


Figure 2: MODIS Terra images (a1-a10) and MODIS aerosol optical depth AOD at 550 nm (b1-b10) showing dust outbreak across East Asia during 22-31 January 2023. Red Rectangular, triangle, star and circle indicate Lanzhou, Beijing, Shanghai and Taiwan. The red circle with dash line indicates the dust plume.

(a)



(b)



(c)

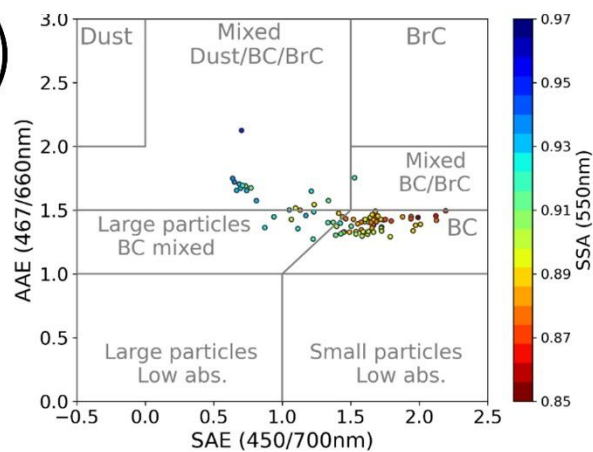


Figure 3: (a) Time series of observed pollutants over LABS during January 2023. The aerosol radiation properties during (b) 24-26 January and (c) 27-30 January 2023.

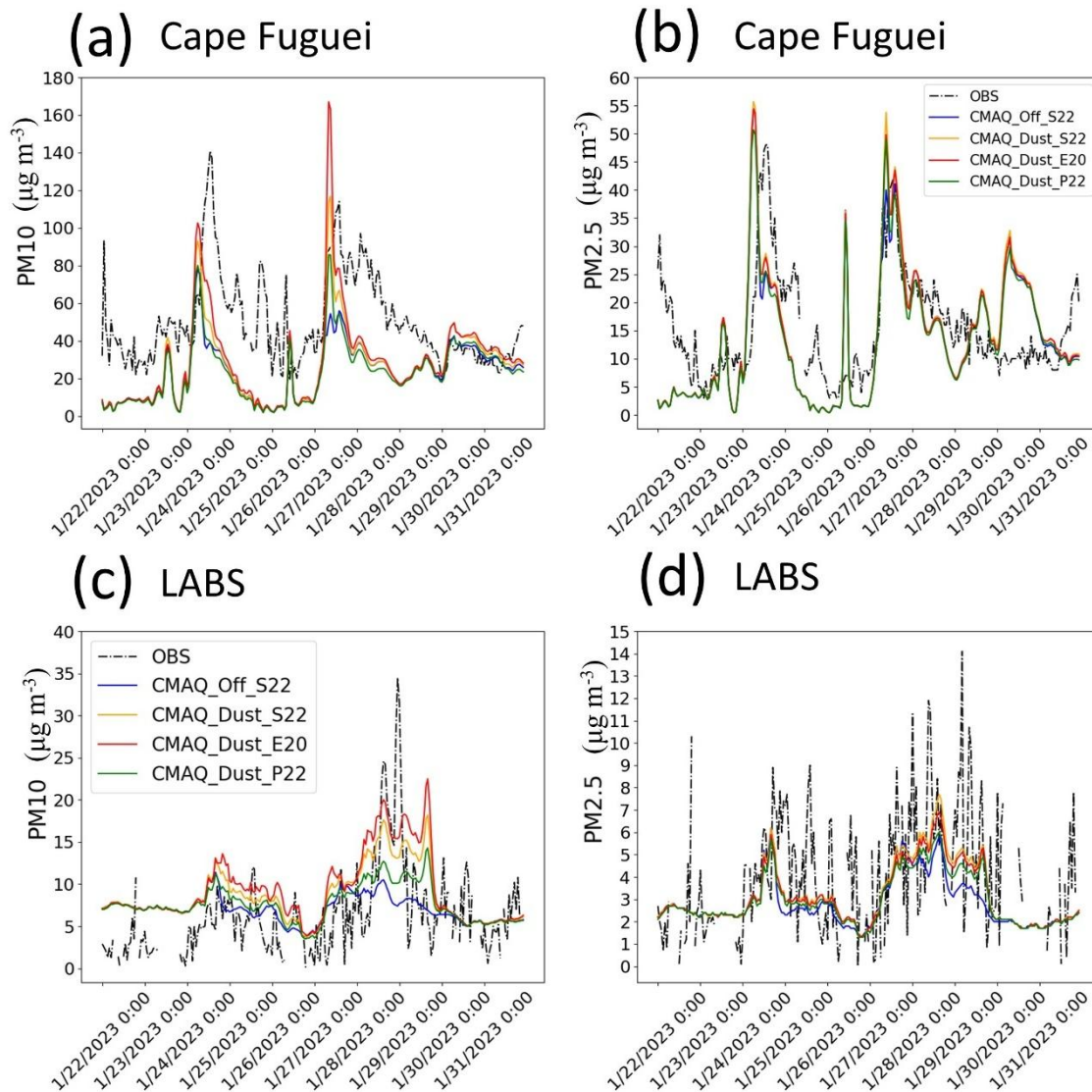
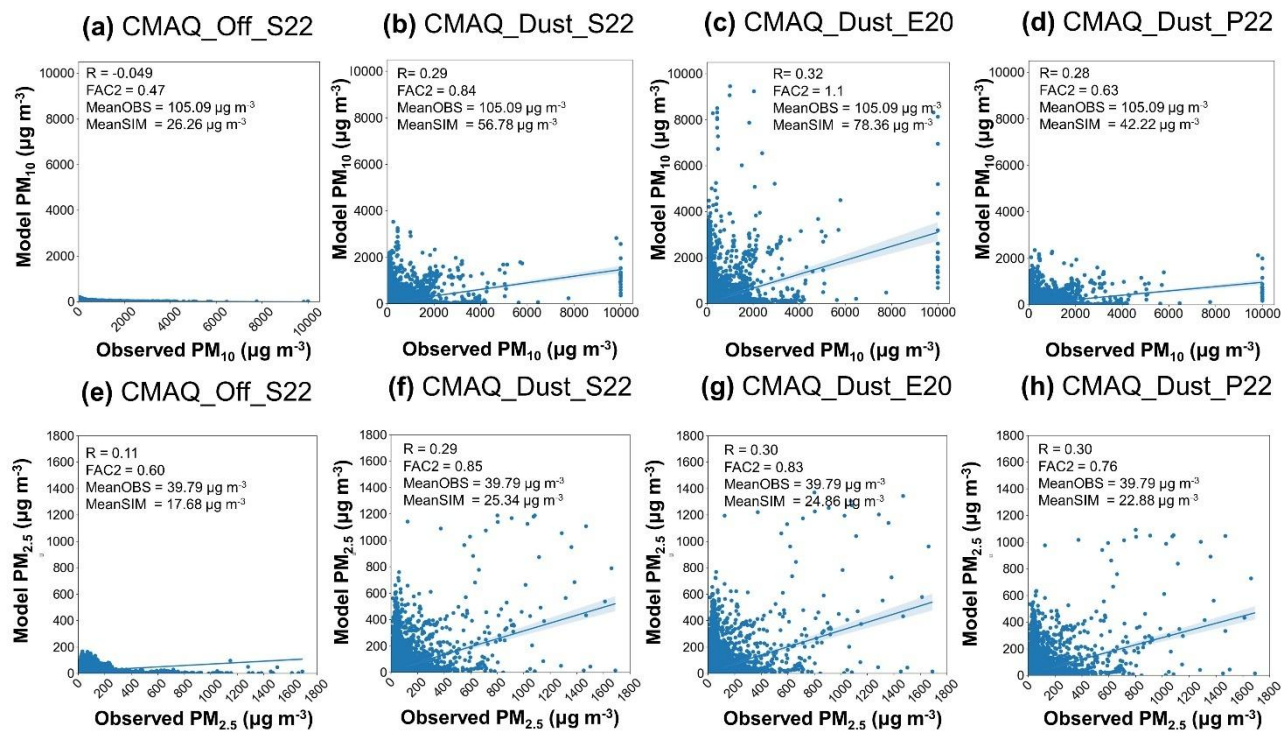
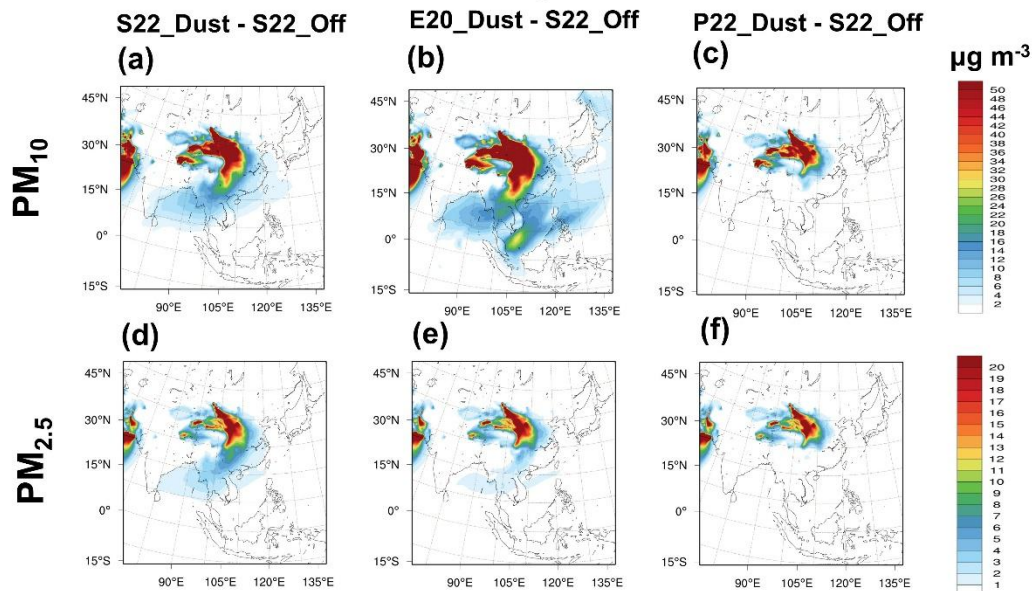


Figure 4: Time series of PM₁₀ (left panel) and PM_{2.5} (right panel) concentrations during 22-31 January 2023 under multiple deposition schemes over the Cape Fuguei (upper panel) and LABS (lower panel), representing the surface and high altitude, respectively.



783
784 **Figure 5:** The scatter plot of the observed against modeled PM_{10} (a-d) and $PM_{2.5}$ (e-h) for
785 CMAQ_Off_S22 (a, e), CMAQ_Dust_S22 (b, f), CMAQ_Dust_E20 (c, g) and CMAQ_Dust_P22 (d, h)
786 at the 100 sites of the mainland China on 12 March-20 April 2021 (<http://>). R is the correlation coefficient
787 between the observation and model; FAC2 is the factor of two; MeanOBS and MeanSIM are the mean of
788 PM from observation and model, respectively.

January 2023



Spring 2021

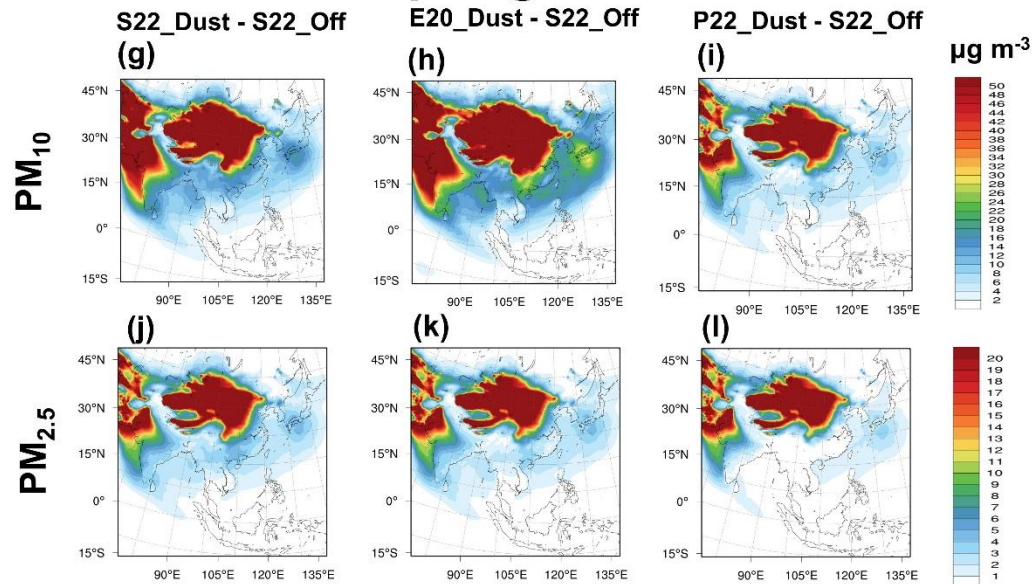


Figure 6: CMAQ estimated 10 days (January 2023) (a-f) and 40 days (Spring 2021) (g-l) averaged mean (a, b, c, g, h, i) PM_{10} and (d, e, f, j, k, l) $PM_{2.5}$ for the concentration changes using (a, d, g, j) S22, (b, e, h, k) E20 and (c, f, i, l) P22 schemes, as relative to the CMAQ_Off_S22 scenarios.

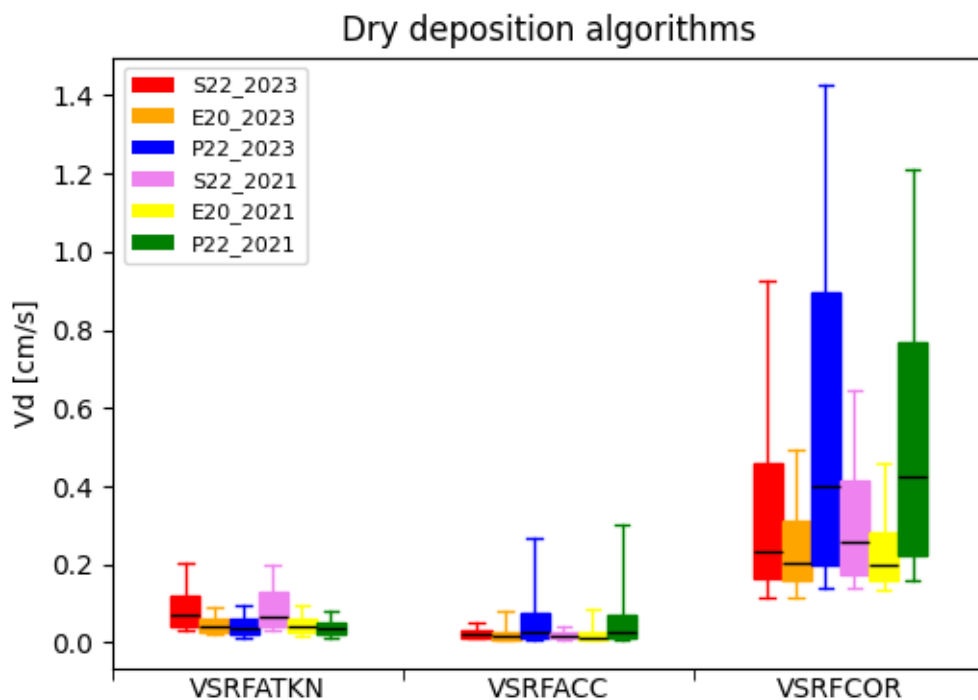


Figure 7: 10-days (2023) and 40-days (2021) averaged dry V_d predicted by CMAQ for the Aitken, accumulation, and coarse particle modes using the 2023_S22 (red), 2023_E20 (orange), 2023_P22 (blue), 2021_S22 (violet), 2021_E20 (yellow) and 2021_P22 (green) particle dry deposition schemes. The variability illustrated by the boxes and whiskers corresponds to spatial variability in annually averaged values throughout the CMAQ domain.

January 2023

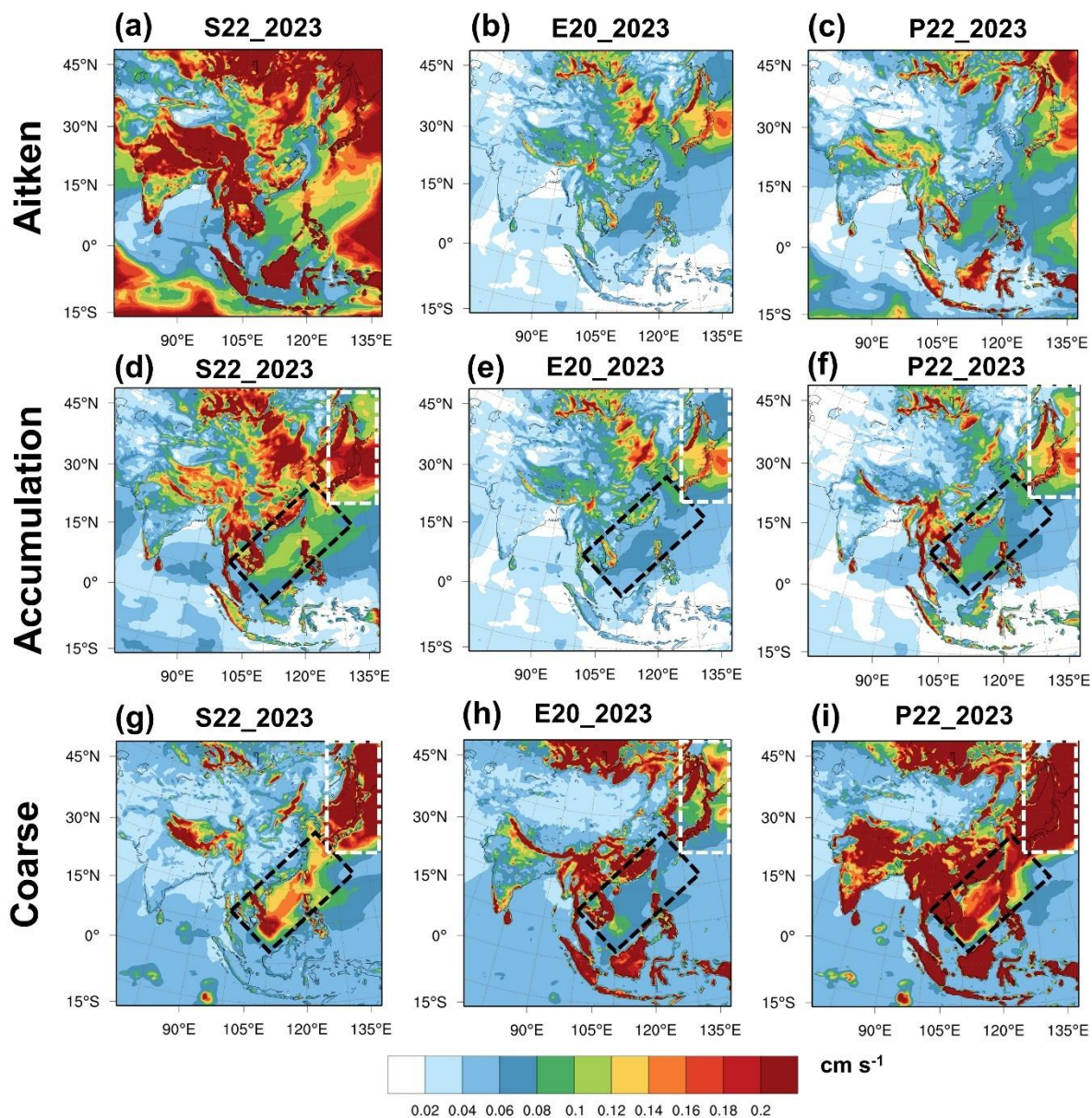
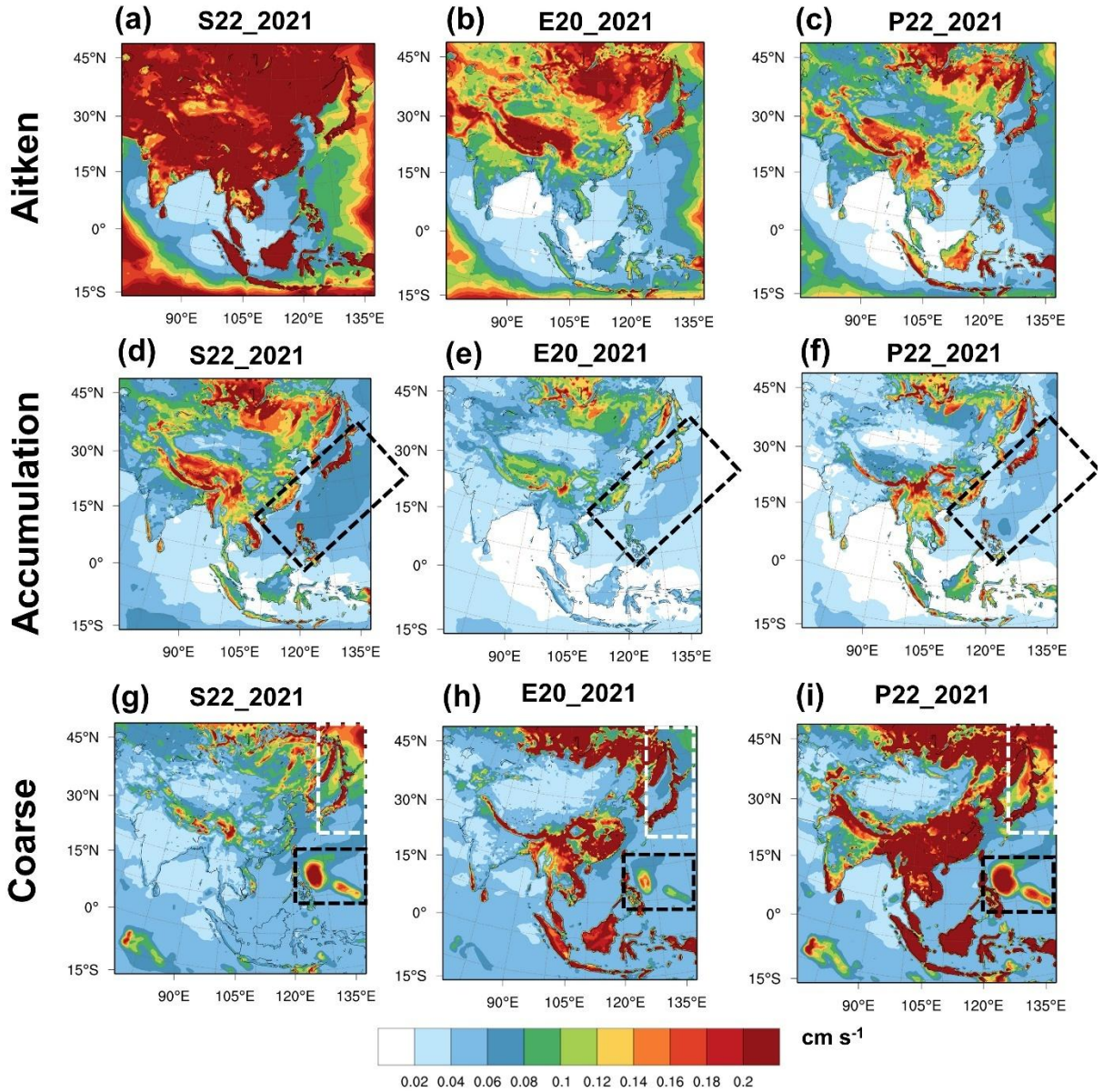


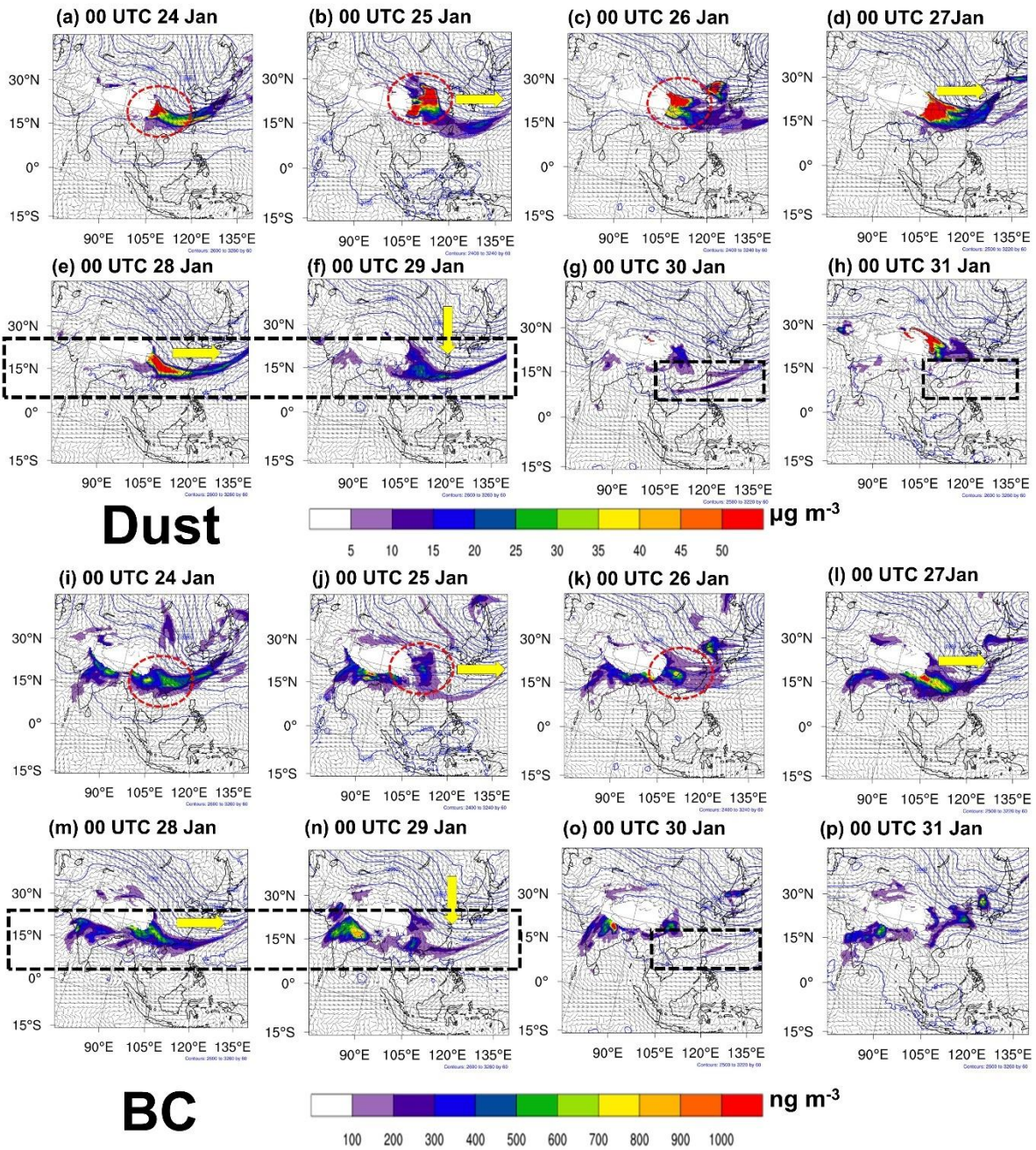
Figure 8: CMAQ estimated 10 days (22-31 January 2023) averaged for the (a-c) Aitken, (d-f) accumulation, and (g-i) coarse particle modes for (a, d, g) S22, (b, e, h) E20, and (c, f, i) P22 dry deposition schemes. White-dash rectangular indicates the region across northwest China; Black-dash rectangular indicates the marine boundary layer at the western Pacific.

Spring 2021



813

814 **Figure 9:** CMAQ estimated 40 days (12 Mar-20 April 2021) averaged for the (a-c) Aitken, (d-f)
 815 accumulation, and (g-i) coarse particle modes for (a, d, g) S22, (b, e, h) E20, and (c, f, i) P22 dry deposition
 816 schemes. White-dash rectangular indicates the region across northwest China; Black-dash rectangular
 817 indicates the marine boundary layer at the western Pacific.



818

819 **Figure 10:** CMAQ_Dust_E20 simulated mineral dust (a-h) and BC aerosol (i-p) concentrations at the
820 700 hPa during 12 UTC 24-31 January 2023. The yellow arrows highlight the trough moving direction.

821 The dash-black rectangular box highlights the aerosol belt.

822

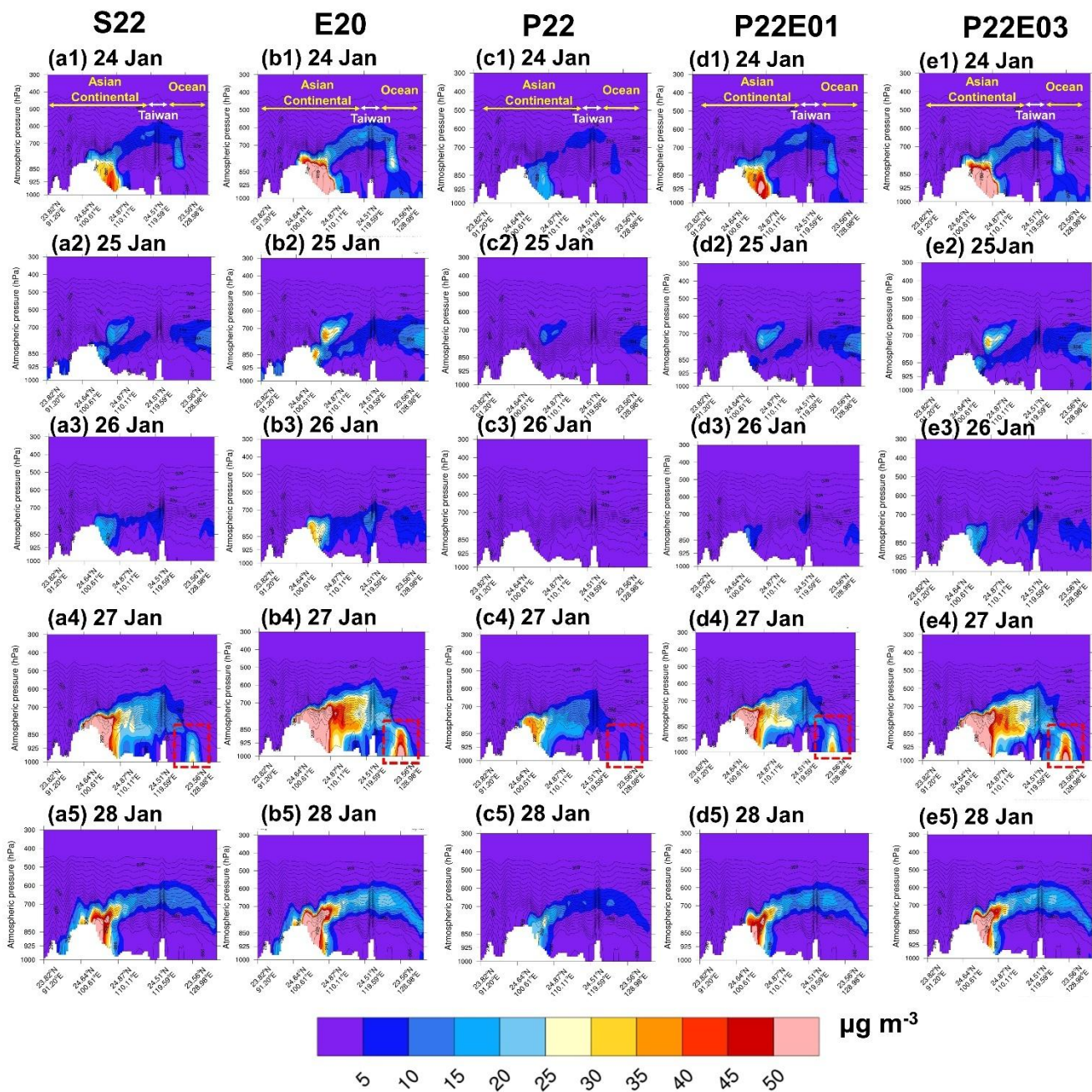


Figure 11: Vertical cross section of the simulated dust aerosol for the CMAQ_DUST (S22, E20, P22, P22E01 and P22E03) during 12 UTC 24-28 January 2023.

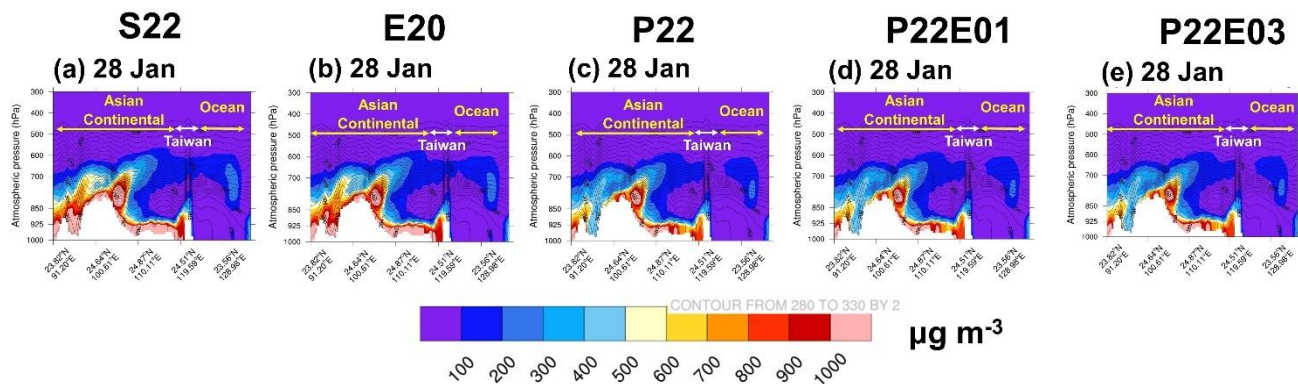


Figure 12: Vertical cross section of the simulated BC aerosol for the CMAQ_DUST (S22, E20, P22, P22E01 and P22E03) during 00 UTC 28 January 2023.

Supplementary Information

Modeling CMAQ dry deposition treatment over Western Pacific: A distinct characteristic of mineral dust and anthropogenic aerosol

Steven Soon-Kai Kong ¹, Joshua S. Fu ², Neng-Huei Lin ^{1,3,*}, Guey-Rong Sheu ^{1,3,*}, Wei-Syun Huang¹

¹ Department of Atmospheric Sciences, National Central University, Taoyuan, 32001, Taiwan

² Department of Civil and Environmental Engineering, the University of Tennessee Knoxville, TN37996, USA

³ Center for Environmental Monitoring and Technology, National Central University, Taoyuan, 32001, Taiwan

880 **Table S1:** V_d percentiles (cm s^{-1}) of atiken, accumulation and coarse particle modes by the three dry
881 deposition schemes.

Dry deposition schemes	Percentiles	Aitken	Accumulation	Coarse
S22	25 th	0.043	0.013	0.163
	50 th	0.069	0.020	0.234
	75 th	0.120	0.033	0.460
E20	25 th	0.026	0.009	0.157
	50 th	0.039	0.014	0.204
	75 th	0.063	0.029	0.312
P22	25 th	0.020	0.012	0.197
	50 th	0.034	0.029	0.401
	75 th	0.062	0.077	0.895

882
883
884
885
886
887
888
889
890

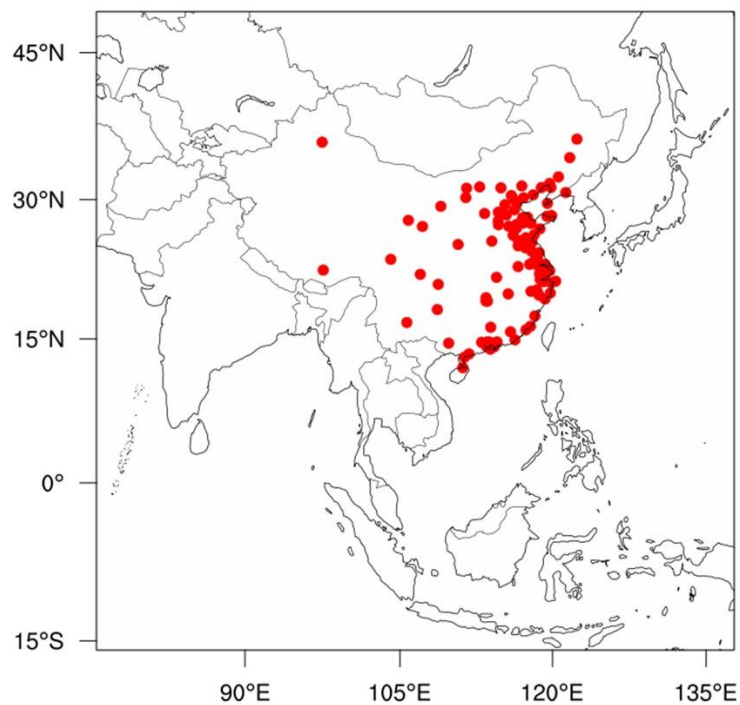


Figure S1: The location of monitoring sites over mainland China used for model evaluation (<http://www.aqistudy.cn/>).

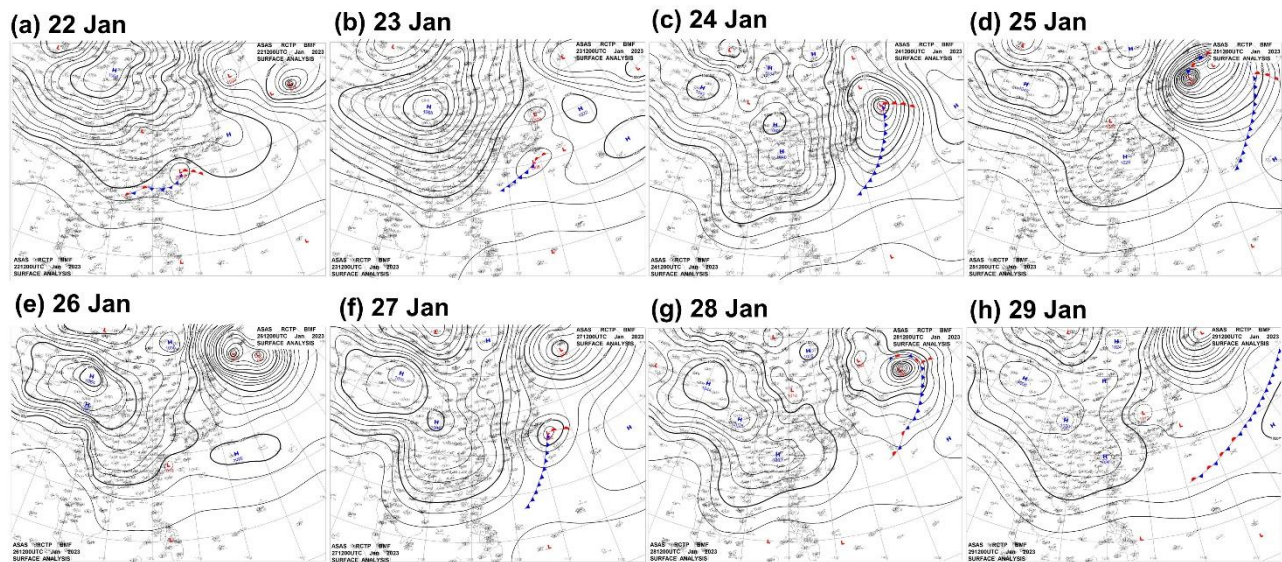


Figure S2: Surface weather maps for the weather pattern obtained by Taiwan Central Weather Bureau (<https://www.cwa.gov.tw/>).

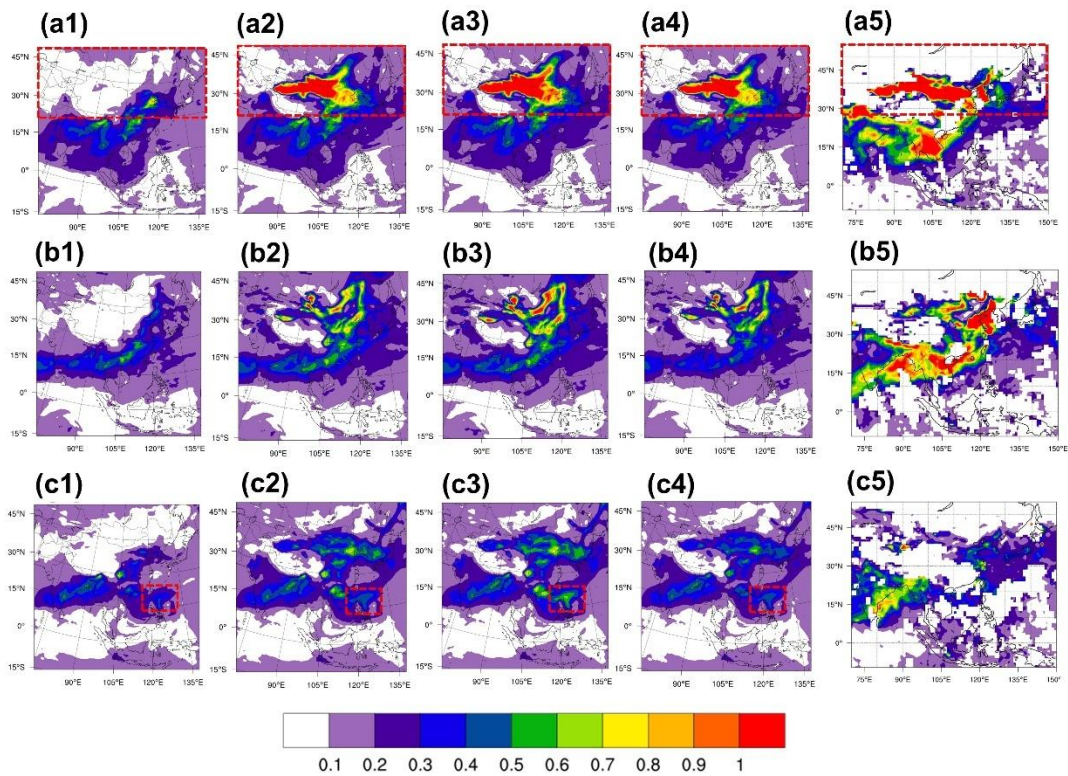


Figure S3: The 3-days mean averaged AOD over East Asia region, for (1-4) CMAQ and (6) MODIS during 14-16 March 2021 (a1-a5), 26-28 March 2021 (b1-b5) and 17-19 April 2021 (c1-c5). The simulations are the CMAQ_Off_S22 (a1, b1, c1), CMAQ_Dust_S22 (a2, b2, c2), CMAQ_Dust_E20 (a3, b3, c3) and CMAQ_Dust_P22 (a4, b4, c4).

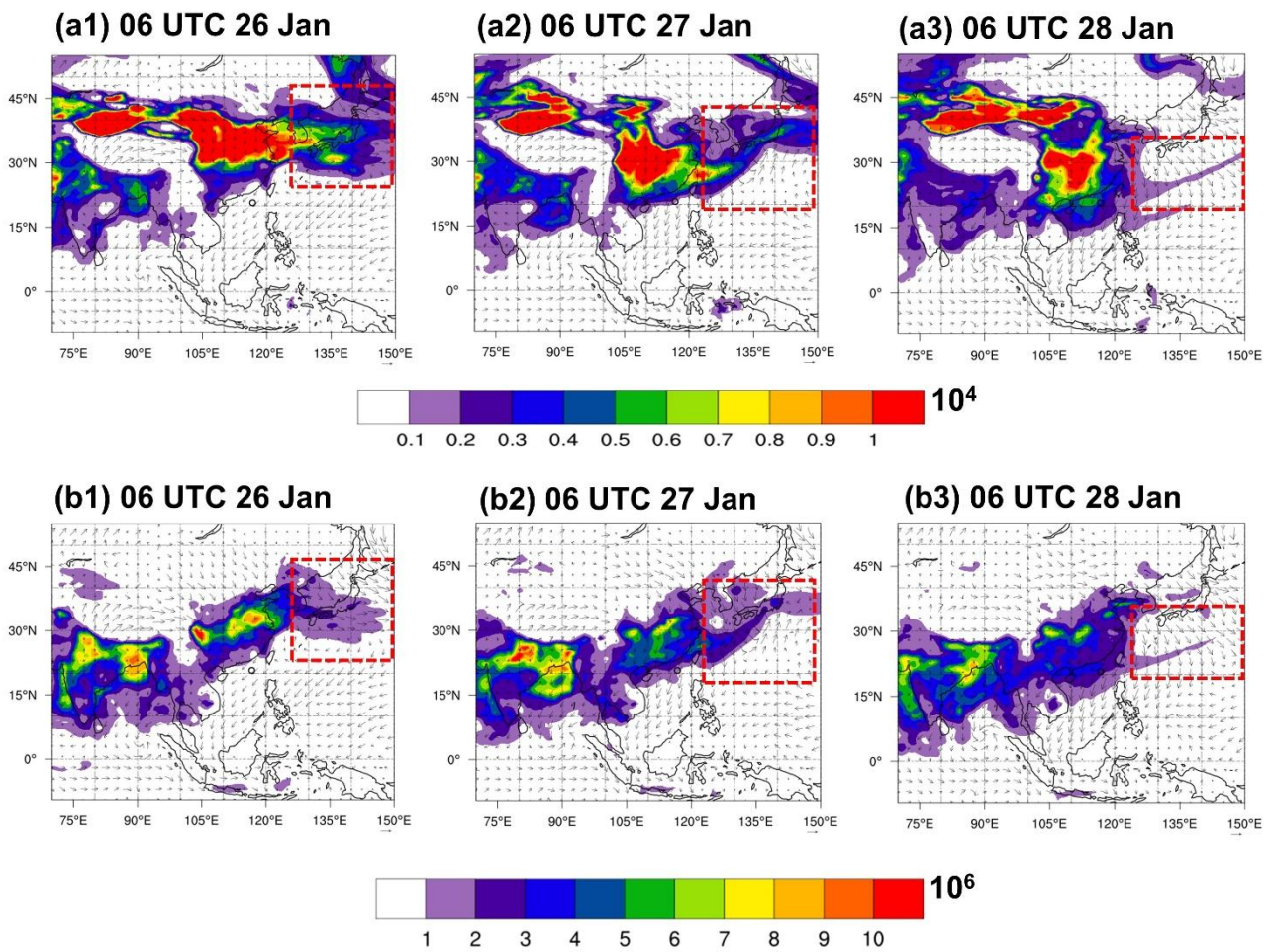


Figure S4: MERRA2 dust (a1-a3) and BC (b1-b3) mass column during 06 UTC (a1, b1) 26 January, (a2, b2) 27 January and (a3, b3) 28 January 2023.